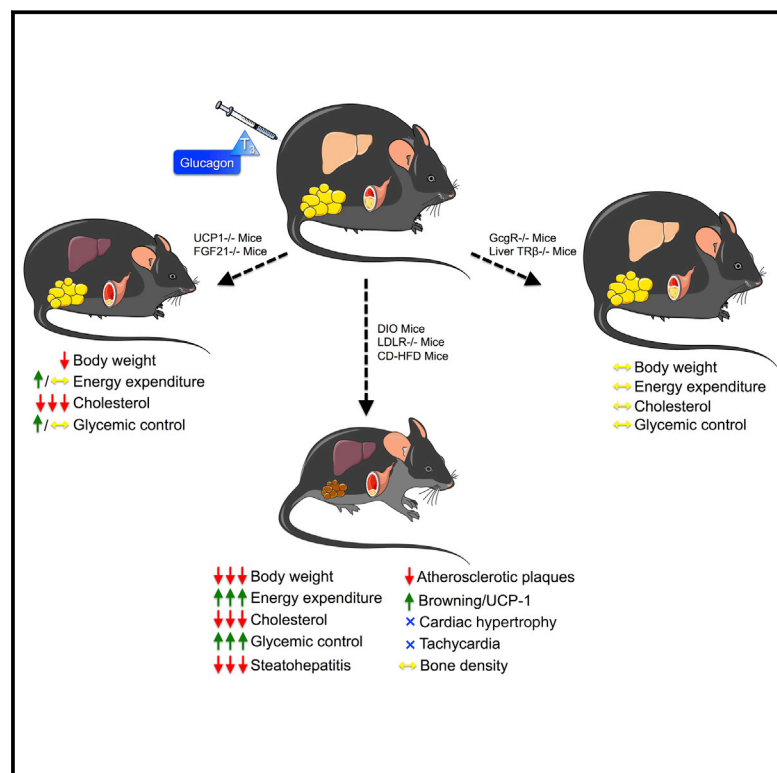# Cell

Chemical Hybridization of Glucagon and Thyroid Hormone Optimizes Therapeutic Impact for Metabolic Disease

Graphical Abstract

Authors

Brian Finan, Christoffer Clemmensen, Zhimeng Zhu, ..., Matthias H. Tschöp, Richard DiMarchi, Timo D. Müller

Correspondence

matthias.tschoep@helmholtz-muenchen. de (M.H.T.), rdimarch@indiana.edu (R.D.)

In Brief

The therapeutic benefits of two hormones are maximized in a synthetic hybrid molecule that treats metabolic syndrome in mice by synergizing favorable effects and off-setting liabilities.

Highlights

- Glucagon/T_3 corrects dyslipidemia, obesity, and hyperglycemia in DIO mice

- Glucagon/T_3 improves NASH and atherosclerosis in preclinical disease models

- Precise delivery of T_3 to the liver mediates benefits and spares cardiac toxicity

- Hepatic T_3 action counteracts the diabetogenic liability of glucagon

Data Resources

GSE85793

CrossMark

CellPress

Article

Cell

Chemical Hybridization of Glucagon and Thyroid Hormone Optimizes Therapeutic Impact for Metabolic Disease

Brian Finan,[1,2,3,25] Christoffer Clemmensen,[1,2,3,25] Zhimeng Zhu,[4] Kerstin Stemmer,[1,2,3] Karine Gauthier,[5] Luisa Müller,[1] Meri De Angelis,[6] Kristin Moreth,[7] Frauke Neff,[7,21] Diego Perez-Tilve,[8] Katrin Fischer,[1,2] Dominik Lutter,[1,2,3] Miguel A. Sánchez-Garrido,[1,2] Peng Liu,[9] Jan Tuckermann,[9] Mohsen Malehmir,[10] Marc E. Healy,[10] Achim Weber,[10] Mathias Heikenwalder,[11,12] Martin Jastroch,[1,2] Maximilian Kleinert,[1,2,22] Sigrid Jall,[1,2] Sara Brandt,[1,2] Frédéric Flamant,[5] Karl-Werner Schramm,[6] Heike Biebermann,[13] Yvonne Döring,[14,23] Christian Weber,[14,24]

(Author list continued on next page)

[1]Institute for Diabetes and Obesity, Helmholtz Diabetes Center at Helmholtz Zentrum München, German Research Center for Environmental Health (GmbH), 85764 Neuherberg, Germany
[2]Division of Metabolic Diseases, Department of Medicine, Technische Universität München, 80333 Munich, Germany
[3]German Center for Diabetes Research (DZD), 85764 Neuherberg, Germany
[4]Department of Chemistry, Indiana University, Bloomington, IN 47405, USA
[5]Institut de Génomique Fonctionnelle de Lyon, Université de Lyon, Centre National de la Recherche Scientifique (CNRS), Institut National de la Recherche Agronomique (INRA), École Normale Supérieure de Lyon, 69364 Lyon, France
[6]Molecular EXposomics, Helmholtz Zentrum München, German Research Center for Environmental Health (GmbH), 85764 Neuherberg, Germany
[7]German Mouse Clinic, Institute of Experimental Genetics, Helmholtz Zentrum München, German Research Center for Environmental Health, 85764 Neuherberg, Germany
[8]Division of Endocrinology, Department of Internal Medicine, Metabolic Diseases Institute, University of Cincinnati College of Medicine, Cincinnati, OH 45237, USA
[9]Institute of Comparative Molecular Endocrinology, University of Ulm, 89081 Ulm, Germany
[10]Department of Pathology and Molecular Pathology, University Zurich and University Hospital Zurich, 8091 Zurich, Switzerland
[11]Institute of Virology, Technische Universität München, 81675 Munich, Germany
[12]Division of Chronic Inflammation and Cancer, German Cancer Research Center (DKFZ), Heidelberg 69120, Germany
[13]Institute of Experimental Pediatric Endocrinology, Charité-Universitätsmedizin Berlin, Berlin 13353, Germany
[14]Department of Medicine, Institute for Cardiovascular Prevention, Ludwig-Maximilians-Universität München, 80336, Munich, Germany
[15]Comprehensive Diabetes Center and Department of Medicine-Endocrinology, Diabetes & Metabolism, University of Alabama at Birmingham, Birmingham, AL 35294, USA
[16]Institute for Diabetes and Regeneration, Helmholtz Diabetes Center at Helmholtz Zentrum München, German Research Center for Environmental Health (GmbH), Neuherberg 85764, Germany
[17]Calibrium LLC, Carmel, IN 46032, USA
[18]Institute for Experimental Endocrinology, Charité-Universitätsmedizin Berlin, Berlin 13353, Germany
[19]Chair of Experimental Genetics, School of Life Science Weihenstephan, Technische Universität München, Freising 85353, Germany

(Affiliations continued on next page)

SUMMARY

Glucagon and thyroid hormone (T_3) exhibit therapeutic potential for metabolic disease but also exhibit undesired effects. We achieved synergistic effects of these two hormones and mitigation of their adverse effects by engineering chemical conjugates enabling delivery of both activities within one precisely targeted molecule. Coordinated glucagon and T_3 actions synergize to correct hyperlipidemia, steatohepatitis, atherosclerosis, glucose intolerance, and obesity in metabolically compromised mice. We demonstrate that each hormonal constituent mutually enriches cellular processes in hepatocytes and adipocytes via enhanced hepatic cholesterol metabolism and white fat browning. Synchronized signaling driven by glucagon and T_3 reciprocally minimizes the inherent harmful effects of each hormone. Liver-directed T_3 action offsets the diabetogenic liability of glucagon, and glucagon-mediated delivery spares the cardiovascular system from adverse T_3 action. Our findings support the therapeutic utility of integrating these hormones into a single molecular entity that offers unique potential for treatment of obesity, type 2 diabetes, and cardiovascular disease.

INTRODUCTION

Dyslipidemia, including hypercholesterolemia and hypertriglyceridemia, represents a hallmark of the metabolic syndrome and triggers a host of obesity-associated comorbidities. Liver

Kirk M. Habegger,[15] Michaela Keuper,[16] Vasily Gelfanov,[4] Fa Liu,[17] Josef Köhrle,[18] Jan Rozman,[3,7] Helmut Fuchs,[7] Valerie Gailus-Durner,[7] Martin Hrabě de Angelis,[3,7,19] Susanna M. Hofmann,[3,16,20] Bin Yang,[4] Matthias H. Tschöp,[1,2,3,*] Richard DiMarchi,[4,26,*] and Timo D. Müller[1,2,3]

[20]Medizinische Klinik und Poliklinik IV, Klinikum der LMU, München 80336, Germany

[21]Institute of Pathology, Helmholtz Zentrum München, German Research Center for Environmental Health, 85764 Neuherberg, Germany

[22]Section of Molecular Physiology, Department of Nutrition, Exercise and Sports, Faculty of Science, University of Copenhagen, 2200 Copenhagen, Denmark

[23]German Centre for Cardiovascular Research (DZHK), partner site Munich Heart Alliance (MHA), 80336 Munich, Germany

[24]Department of Biochemistry, Cardiovascular Research Institute Maastricht (CARIM), Maastricht University, 6200 MD Maastricht, The Netherlands

[25]Co-first author

[26]Lead Contact

*Correspondence: matthias.tschoep@helmholtz-muenchen.de (M.H.T.), rdimarch@indiana.edu (R.D.)

http://dx.doi.org/10.1016/j.cell.2016.09.014

and adipose tissues orchestrate systemic lipid homeostasis, and reciprocal dysfunction in these organs propels a vicious cycle of metabolic derangements. Hepatic steatosis is a key pathogenic factor in hepatic insulin resistance and non-alcoholic fatty liver disease (NAFLD), and perturbed cholesterol handling accelerates atherosclerosis, thus positioning dyslipidemia at the interface of type 2 diabetes (T2D) and coronary heart disease (CHD).

Inhibiting hepatic cholesterol synthesis via statins provides clinically relevant reductions in circulating cholesterol and proportionally lowers CHD risk (Nicholls et al., 2011). However, a considerable number of patients still fail to meet target reductions in cholesterol, and a significant limitation of statin therapy is its near exclusive focus on cholesterol lowering with no benefit to glycemic control or body weight (Diamond and Ravnskov, 2015). Therefore, a pharmacological agent that lowers cholesterol, triglycerides, glucose, hepatic fat, and body weight would offer a transformative advancement for treatment of the metabolic syndrome that should decrease mortality risk from cardiovascular events.

Thyroid hormones powerfully influence systemic metabolism through multiple pathways, with profound effects on energy expenditure, fat oxidation, and cholesterol metabolism (Mullur et al., 2014). However, adverse side effects of thyroid hormone treatment include increased heart rate, cardiac hypertrophy, muscle wasting, and reduced bone density (Ochs et al., 2008). Discovery of thyromimetics capable of separating lipid metabolism benefits from adverse cardiovascular effects has remained a desire. This guided attempts to rationally design small molecules with selective preference for thyroid hormone receptor beta (TRβ) to treat dyslipidemia without inducing cardiac damage (Grover et al., 2003). Second generation thyromimetics sought isoform specificity and tissue-specific function by derivatization with chemical moieties to promote tissue selectivity. These liver-targeted thyromimetics initially showed promising pre-clinical effects on handling hepatic lipids and atherogenic lipoproteins. No loss in body weight has been achieved as their mechanism of liver-targeting precludes lipolytic effects in adipose tissue (Baxter and Webb, 2009). Therefore, selective but broadened thyroid hormone action that includes liver and adipose depots, yet spares the cardiovascular system, could offer comprehensive metabolic benefit.

Glucagon also offers many benefits for metabolic diseases independent from its glycemic effects, including lowering lipids in circulation and in the liver (Habegger et al., 2010). The benefits of glucagon action are not solely constrained to the liver as adipose tissue is a secondary target organ for glucagon action to promote lipolysis and energy expenditure through thermogenic mechanisms (Habegger et al., 2010). These coordinated actions demonstrate the validity of glucagon-based agonists as an anti-obesity therapy, but only if the inherent diabetogenic liability can be properly controlled (Habegger et al., 2013). We have shown that the hyperglycemic propensity of unopposed glucagon action can be effectively counterbalanced by incorporating incretin peptide activity into a glucagon-based single peptide, including unimolecular mixed agonists with glucagon-like peptide-1 (GLP-1) (Day et al., 2009) and/or glucose-dependent insulinotropic polypeptide (GIP) (Finan et al., 2013, 2015).

Here, we envisioned that we could turbo-charge the liver-mediated lipid-lowering properties of glucagon, as well as the adipose-mediated thermogenic properties of glucagon, by introducing thyroid hormone activity into a single molecule, glucagon-based mixed agonist. We envisioned that this approach could also unleash the therapeutic utility of thyroid hormone by selectively targeting its action profile to liver and adipose tissue with a glucagon shuttle. Our vision gained momentum when we recently succeeded with an approach that allowed us to selectively, efficiently, and safely target estrogen action to the hypothalamus and pancreas using GLP-1 as a shuttle (Finan et al., 2012; Tiano et al., 2015; Schwenk et al., 2015). We have expanded that technology to include other hormonal combinations. Here, we report glucagon-mediated selective delivery of thyroid hormone to the liver results in coordinated actions that synergize to correct hyperlipidemia, reverse hepatic steatosis, and lower body weight through liver- and fat-specific mechanisms. Importantly, the liver-directed thyroid hormone action overrides the diabetogenic liability of local glucagon action resulting in a net improvement of glycemic control, while glucagon-mediated delivery spares adverse action of thyroid hormone, notably on the cardiovascular system.

RESULTS

Generation of Glucagon and Thyroid Hormone Conjugates

We rationally designed a series of unimolecular conjugates of glucagon and thyroid hormone. We used a 40-mer glucagon analog that we rendered resistant to dipeptidyl peptidase IV
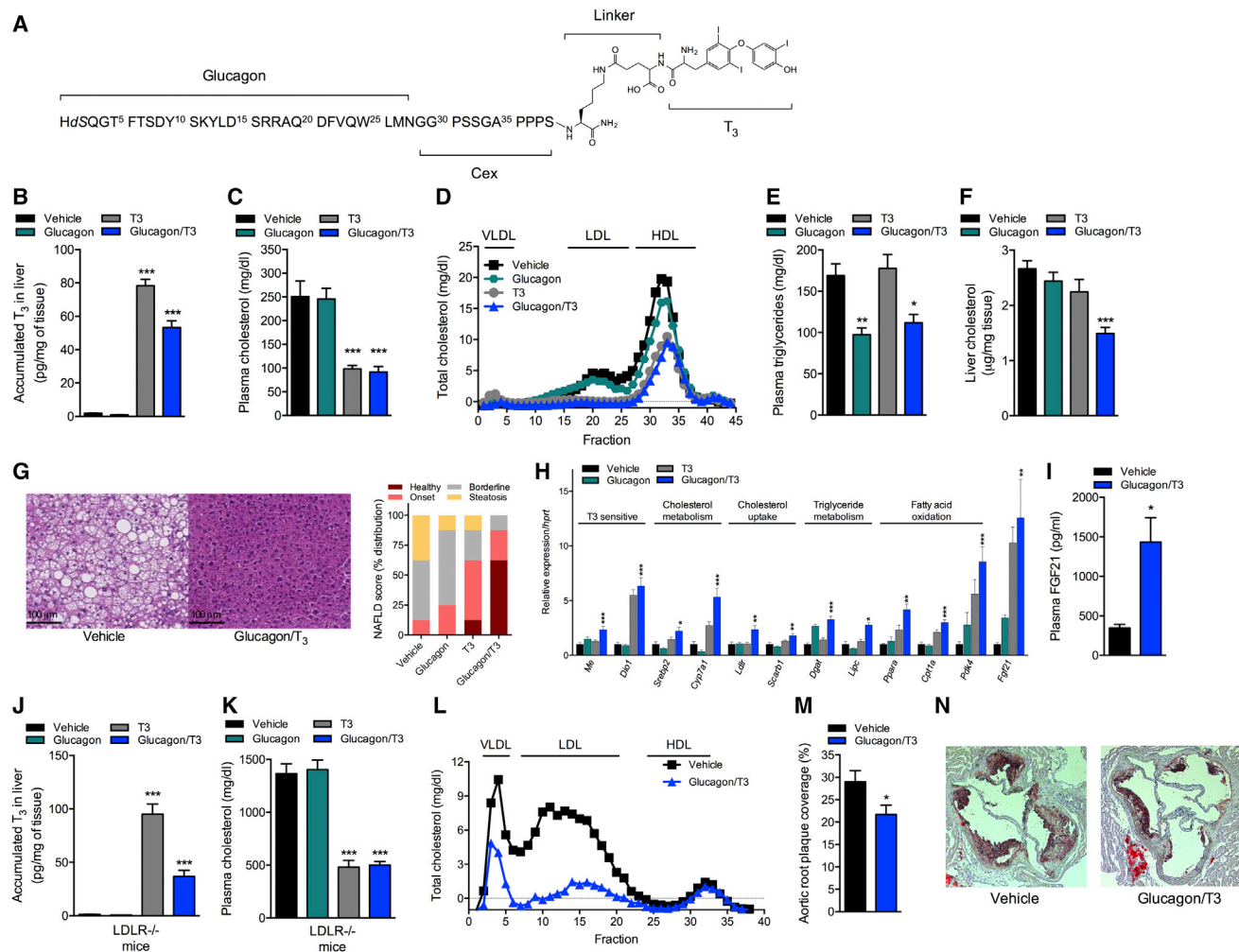
Figure 1. Glucagon/T$_3$ Improves Dyslipidemia and Ameliorates Atherosclerosis in Western Diet-Fed Mice

(A) Sequence and structure of glucagon/T$_3$.

(B–I) Effects on (B) levels of hepatic T$_3$, plasma levels of (C) total cholesterol, (D) cholesterol bound to different lipoprotein fractions, (E) triglycerides, (F) hepatic cholesterol, (G) liver H&E staining and steatosis score, (H) hepatic mRNA profile, and (I) plasma levels of FGF21 from HFHCD-fed male C57Bl6j mice following daily s.c. injections of vehicle (black), a glucagon analog (teal), T$_3$ (gray), or glucagon/T$_3$ (blue) at a dose of 100 nmol kg^{-1} for 14 days (n = 8).

(J–N) Effects on (J) hepatic levels of T$_3$, plasma levels of (K) total cholesterol, (L) cholesterol bound to different lipoprotein fractions, (M) percentage of oil-red O-positive area per total area in the aortic root, and (N) representative images of oil-red O staining of aortic root sections from HFHCD-fed LDLR$^{-/-}$ male mice following daily s.c. injections of vehicle (black), a glucagon analog (teal), T$_3$ (gray), or glucagon/T$_3$ (blue) at a dose of 100 nmol kg^{-1} for 14 days (n = 8).

*p < 0.05, **p < 0.01, and ***p < 0.001 comparing effects following compound injections to vehicle injections. All data are presented as mean ± SEM.

See also Figures S1, S2, S3, and S4.

degradation and C-terminally extended by 11 residues as the peptide backbone to make conjugates of glucagon and T$_3$ (Figure S1A). This 40-mer glucagon analog, herein referred to as just glucagon, has a comparable in vitro activity profile at GcgR as native glucagon (Figure S1B). We constructed three different glucagon/thyroid hormone conjugates. Two of these conjugates include the most bioactive form of thyroid hormone, 3,3′,5-triiodothyronine (T$_3$). In the first conjugate, herein referred to as "glucagon/T$_3$," the T$_3$ moiety is covalently attached to the side chain amine of the C-terminal lysine through a gamma glutamic acid (γGlu) spacer added to the carboxylate of T$_3$ (Figures 1A and S1C). In the second conjugate, the amine of T$_3$ is covalently

linked to the peptide through a succinate spacer at this terminal lysine (Figure S1D). The molecular orientation of the T$_3$ is inverted relative to the first conjugate (glucagon/T$_3$) and is herein referred to as "glucagon/iT$_3$." For the third conjugate, 3,3,5′-triiodothyronine was used, otherwise called reverse T$_3$ (rT$_3$), an inactive metabolite of thyroid hormone. The rT$_3$ was coupled to glucagon with the same linker chemistry as used with glucagon/T$_3$ to generate the conjugate referred to as "glucagon/rT$_3$" (Figure S1E). Mass spectral analysis for each compound is presented in Figures S2A–S2D. The three different conjugates have similar activity as the parent peptide at GcgR (Figure S2E) yet only glucagon/T$_3$ elicited transcriptional activity of a thyroid hormone response element in

HepG2 cells that express GcgR (Figure S2F). This is presumably through hydrolysis in the γGlu spacer to release T_3, which is not evident with glucagon/iT3 (Figure S2G). Importantly, glucagon/T_3 remains intact with nearly no detectable degradation in the presence of human plasma at 37°C for up to 24 hr (Figures S2H–S2J).

Glucagon/T_3 Synergistically Improves Hepatic Cholesterol and Lipid Handling

To determine whether glucagon-mediated delivery of T_3 can reverse dyslipidemia and hepatic steatosis in metabolically compromised mice, we administered the glucagon/T_3 conjugates, along with mono-agonist controls, to mice maintained on a high-fat, high-cholesterol diet (HFHCD). After chronic treatment, the amount of T_3 observed in the liver increased following treatment with glucagon/T_3 and matches that observed with T_3 mono-therapy (Figure 1B). Liquid chromatography-mass spectrometry (LC-MS) was used to quantify the amount of T_3 that accumulated in the liver after chronic treatment, thus it is confirmed that native T_3 is released from the conjugate. Glucagon/T_3 lowered levels of total plasma cholesterol in a dose-dependent manner with an onset as early as 4 days of treatment (Figure S3A). At the highest dose and similar to T_3, glucagon/T_3 reduced circulating levels of total cholesterol (Figures 1C and S3A) and the fraction of cholesterol bound to both low-density lipoproteins (LDL) and high-density lipoproteins (HDL) (Figure 1D). Glucagon/T_3 reduced circulating levels of triglycerides to a similar extent as the glucagon analog (Figure 1E). Glucagon/T_3 lowered hepatic cholesterol content (Figure 1F) and hepatocellular vacuolation (Figure 1G) compared to vehicle controls. Plasma levels of alanine aminotransferase (ALT) and aspartate aminotransferase (AST) (Figure S3D), urea nitrogen (Figure S3E), and creatinine (Figure S3F) were unchanged. Plasma levels of ketone bodies (Figure S3G) and citrate synthase activity (Figure S3H) were elevated with glucagon/T_3 treatment. These beneficial effects of glucagon/T_3 on dyslipidemia were similar to the effects observed after equimolar co-administration of glucagon and T_3 (Figures 1C–1E, S4A, and S4B), demonstrating that both constituent actions are responsible for the combined effects on lipids of the conjugate. The cholesterol lowering effect, which is mostly attributable to T_3 action, was not evident after treatment with glucagon/iT$_3$ or glucagon/rT$_3$ (Figures S4A and S4B). This demonstrates that the specific form of thyroid hormone and its molecular orientation are vital for eliciting the coordinated hormonal actions. The effect to lower plasma cholesterol is greater than the effect observed with equimolar treatment of two thyromimetics (GC-1 and KB-2115) selective for TRβ whereas the effects on plasma triglycerides are comparable (Figures S4C and S4D). We therefore exclusively used glucagon/T_3 as the conjugate for preclinical assessment of coordinated glucagon and T_3 action in vivo.

We analyzed the livers from these mice for genes involved in cholesterol and lipid metabolism (Figures 1H and S3I). Glucagon/T_3 increased the expression of key genes involved in cholesterol metabolism and uptake, fatty acid oxidation, and triglyceride cycling. Glucagon/T_3 also increased mRNA expression and plasma levels of fibroblast growth factor 21 (FGF21; Figures 1H and 1I). These changes in lipid metabolism gene programs reflect integrated hormonal actions that resulted in decreased levels of cholesterol and lipids in circulation and in the liver.

Glucagon/T_3 Improves Lipid Handling and Ameliorates Atherosclerosis in $Ldlr^{-/-}$ Mice

To test in a murine model that more closely resembles human physiology of exaggerated dyslipidemia and to parse out cholesterol-lowering mechanisms, we used low-density lipoprotein receptor knockout mice ($Ldlr^{-/-}$). Both the hepatic accumulation of T_3 (Figure 1J) and lowered plasma cholesterol following glucagon/T_3 treatment was confirmed in $Ldlr^{-/-}$ mice (Figure 1K). The conjugate primarily lowered cholesterol stored in the very low-density lipoprotein (VLDL) and LDL fractions without influencing HDL levels (Figure 1L). Beyond the translational relevance, this finding indicates that complementary mechanisms independent of LDLR-mediated uptake contribute to the overall efficacy in cholesterol-lowering.

Because $Ldlr^{-/-}$ mice display atherosclerotic plaque development and aortic lesions similar to human pathophysiology, we explored whether glucagon/T_3 can reverse atherosclerotic plaque formation in $Ldlr^{-/-}$ mice. In this restorative treatment paradigm, 2 weeks of treatment with glucagon/T_3 reduced atherosclerotic plaque size and lesion coverage at the aortic root compared to vehicle-treated controls (Figures 1M and 1N). Our results demonstrate that glucagon/T_3 improves lipid metabolism to an extent that leads to the regression of established atherosclerosis.

Glucagon Drives the Pharmacokinetics of Glucagon/T_3 and Predominantly Traffics to the Liver

To determine if the covalent attachment of T_3 to glucagon alters the pharmacokinetics of the parent molecules, we measured the plasma half-life of the administered compounds following a single bolus subcutaneous (s.c.) injection to lean rats. The pharmacokinetic profile of glucagon/T_3 more closely resembles the profile of the glucagon analog as opposed to native T_3 (Figure S5A). Therefore, altered pharmacokinetics are not contributing to the enhanced pharmacodynamics delivered by glucagon/T_3.

To determine the tissue selectivity of glucagon/T_3, we labeled glucagon/T_3 with the fluorescent probe on the peptide backbone. The labeling of glucagon/T_3 (herein called glucagon*/T_3) did not influence in vitro GcgR activity (glucagon/T_3 EC$_{50}$ = 0.050 nM and glucagon*/T_3 EC$_{50}$ = 0.058 nM), or serum half-life (Figure S5B). Plasma level of glucagon*/T_3 peaked within 3 hr and was cleared by the kidneys within 24 hr (Figure S5C). Whereas the dye control is rapidly cleared from the liver, glucagon*/T_3 presence in the liver persisted and maintained an elevated signal even after it was completely cleared from plasma and urine (Figures 2A and 2B). We observed that glucagon*/T_3 preferentially targets the liver (Figure S5D), and substantially lesser signals were detected in the pancreas, inguinal fat, and heart. This tissue accumulation pattern largely overlaps with the mRNA profile of mouse $Gcgr$ (Figure S5E). Cumulatively, glucagon is the dominant constituent that determines exposure and biodistribution, with liver as the predominant site of action.

Lipid Handling Benefits Are Co-mediated by GcgR and TRβ and Independent from FGF21

To exclude off-target effects and examine the contribution of each component to the lipid lowering effects, we administered glucagon/T_3 to global GcgR knockout mice ($Gcgr^{-/-}$ mice) as
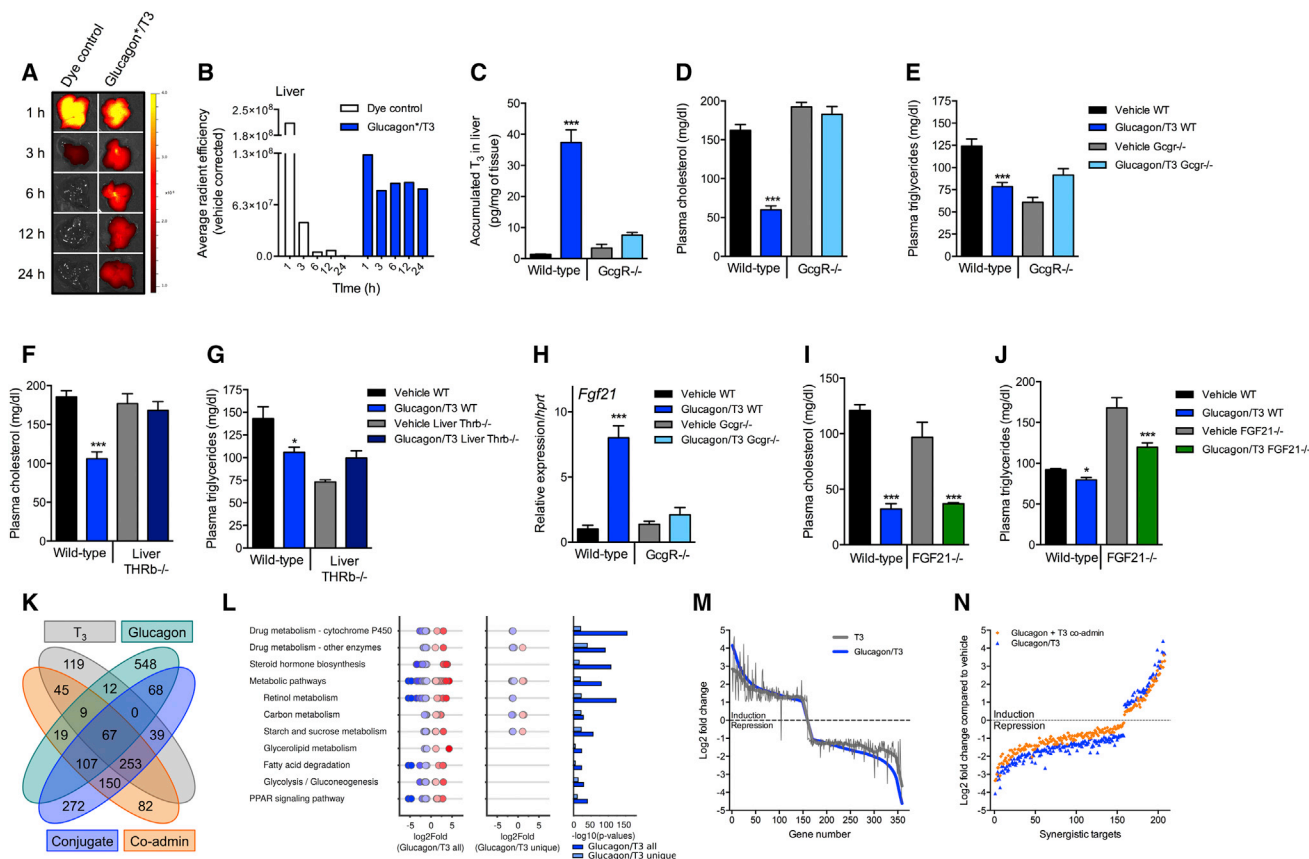
Figure 2. Hepatic Transcript Signature and Hepatic Lipid Improvements of Glucagon/T₃ Require GcgR and THRβ but Not FGF21

(A and B) Epifluorescent signal (A) and quantified average radiant efficiency (B) in livers over time following a single s.c. injection of vehicle, unconjugated dye control, or fluorescently labeled glucagon/T₃ (glucagon*/T₃) at a dose of 100 nmol kg⁻¹ in lean, chow-fed C57Bl6j mice.

(C–E and H) Effects on (C) hepatic levels of T₃, plasma levels of (D) total cholesterol and (E) triglycerides, and (H) relative expression *fgf21* in livers from HFHSD-fed global GcgR⁻/⁻ male mice following daily s.c. injections of vehicle or glucagon/T₃ at a dose of 100 nmol kg⁻¹ for 7 days (n = 7–9).

(F and G) Effects on plasma levels of (F) total cholesterol and (G) triglycerides from HFHCD-fed Alf-THRβ⁻/⁻ male mice following daily s.c. injections of vehicle or glucagon/T₃ at a dose of 100 nmol kg⁻¹ for 7 days (n = 5–7).

(I and J) Effects on plasma levels of (I) total cholesterol and (J) triglycerides from HFHSD-fed global FGF21⁻/⁻ male mice following daily s.c. injections of vehicle or glucagon/T₃ at a dose of 100 nmol kg⁻¹ for 7 days (n = 8).

(K–N) RNA-seq analysis of livers from HFHCD-fed C57BL/6j male mice (n = 4) following 14 days of treatment with vehicle, a glucagon analog, T₃, co-administration of the glucagon analog and T₃, and the glucagon/T₃ conjugate. (K) Overlap of genes significantly regulated (>2-fold change) by the different treatment groups compared to vehicle controls. (L) Top pathways enriched in the liver by treatment with glucagon/T₃ with associated –log10 p values (right graph) for all (blue) and uniquely (green) regulated by glucagon/T₃. Each dot displays one significant regulated gene/transcript mapped to the pathway shown with color codes for up- (red) and downregulation (blue). (M) Comparison of the magnitude of the fold change in transcription between similar genes regulated by both T₃ alone and glucagon/T₃. (N) Magnitude of the fold change in transcription between targets that are regulated in the same direction by co-administration compared to glucagon/T₃. To detect for synergistic like effects, we calculated a synergy score (SS) (see the STAR Methods details) for each expressed transcript and found 208 synergistic targets. For each target the log2FC for treatment with glucagon + T₃ co-admin and glucagon/T₃ is shown.

*p < 0.05, **p < 0.01, and ***p < 0.001 comparing effects following compound injections to vehicle injections within each genotype. All data are presented as mean ± SEM.

See also Figure S5.

well as to liver-specific TRβ knockout mice (liver-specific *Thrb⁻/⁻*). Levels of T₃ in the livers of *Gcgr⁻/⁻* mice were not increased relative to wild-type counterparts following glucagon/T₃ treatment (Figure 2C). The effects to lower cholesterol and triglycerides were absent in *Gcgr⁻/⁻* mice (Figure 2D–2E) and liver-specific *Thrb⁻/⁻* mice (Figure 2F–2G) compared to wild-type mice. The absence of such effects in both knockout lines demonstrates the target specificity and liver preference of glucagon/T₃ to govern the effects on cholesterol and triglyceride

metabolism. Further, glucagon activity is essential for sufficient T₃ delivery and TRβ is responsible for coordinating improved lipid handling.

Hepatic action of FGF21 works to improve lipid metabolism in rodents (Fisher et al., 2011) and this bioactivity translates to humans (Gaich et al., 2013; Talukdar et al., 2016). Given that glucagon/T₃ stimulated a robust expression and induction of FGF21 (Figures 1H and 1I) that was silenced in GcgR⁻/⁻ mice (Figure 2H), we studied the contribution of FGF21 to

the metabolic benefits delivered by glucagon/T$_3$ using germline FGF21 knockout (*Fgf21*$^{-/-}$) mice. The lipid-lowering effects of glucagon/T$_3$ do not appear to be facilitated through FGF21 as plasma levels of cholesterol and triglycerides were decreased by glucagon/T$_3$ in *Fgf21*$^{-/-}$ mice (Figures 2I and 2J).

Glucagon-Targeted T$_3$ Adjusts Hepatic Gene Programs More Efficiently Than Individual Agonists

RNA sequencing (RNA-seq) of livers revealed that glucagon/T$_3$ regulated the expression of 956 genes with at least a 2-fold change compared to vehicle (Figure 2K). Mapping identified "steroid hormone biosynthesis" and "metabolic pathways" as two functional patterns that were differentially regulated in the livers of glucagon/T$_3$-treated mice relative to vehicle (Figure 2L). The subcategories of "metabolic pathways" that were enriched included many specific gene programs involved in lipid and carbohydrate metabolism (Figure 2L). Our analysis of the transcriptomic response also uncovered 359 genes that were regulated by T$_3$ alone and 242 genes that only responded to glucagon (Figure 2K). A total of 577 genes were similarly regulated by glucagon/T$_3$ and the co-administration of glucagon and T$_3$ (Figure 2K). This substantial overlap demonstrates that both glucagon-sensitive and T$_3$-sensitive signaling events are being engaged in the liver by the glucagon/T$_3$ conjugate. The magnitude of the regulation of those T$_3$-sensitive genes (that are those 359 targets identified above as T$_3$-sensitive) was stronger with the conjugate compared to T$_3$ alone (Figure 2M). Indeed, we observe that the conjugate synergistically regulates gene expression of targets that are modulated by both co-administration and the conjugate (Figure 2N). To quantify this, we applied a synergy score (see the STAR Methods) on just those targets that are regulated in the same direction by the conjugate and co-administration. This independent analysis shows that for those 208 genes, the magnitude of regulation is conspicuously greater with the conjugate than with glucagon and T$_3$ co-administration, supporting the notion that cumulative targeting may translate to enhanced therapeutic impact. Interestingly, 272 genes were uniquely regulated by glucagon/T$_3$, but did not respond to single or co-administration of glucagon and T$_3$ (Figure 2K), suggesting that novel signaling cues are being engaged. Sub-analysis of these uniquely regulated 272 genes largely recapitulated the pathways enriched in the 956 genes differentially expressed by glucagon/T$_3$, and no new pathways were enriched within this select pool of transcripts (Figure 2L).

### Glucagon/T$_3$ Improves Liver Health in Mouse Model of Nonalcoholic Steatohepatitis

Because glucagon/T$_3$ substantially improved hepatic fat content in mice fed HFHCD, we next explored if the conjugate could ameliorate signs of steatohepatitis in a rodent model of NAFLD-induced nonalcoholic steatohepatitis (NASH) and metabolic syndrome. Mice maintained on a choline-deficient, high-fat diet (CD-HFD) for 6 months, which has been shown to be sufficient time to develop hallmark signs of human NASH (Wolf et al., 2014), were treated with glucagon/T$_3$ for 3 weeks. Glucagon/T$_3$ normalized serum levels of cholesterol (Figure 3A),

lowered triglycerides (Figure 3B), improved blood glucose (Figure 3C), and reduced body weight (Figure 3D) without affecting blood parameters or blood immune cells (Table S1) relative to vehicle-treated controls. Glucagon/T$_3$ treatment resulted in a substantial lowering of serum ALT concentrations (Figure 3E), suggesting an improvement in liver damage, which was confirmed by macroscopic and histological analysis (Figure 3F). H&E staining and Sudan red staining of liver sections illustrated decreased steatosis by glucagon/T$_3$, including a reduction in the overall area covered by Sudan red positive lipid droplets, ballooned hepatocytes, and satellitosis (Figures 3F and 3G). Although only relatively mild pericellular fibrosis was observed in livers of vehicle-treated mice, virtually no signs of fibrosis were observed in livers from mice treated with glucagon/T$_3$ (Figure 3F).

Glucagon/T$_3$ Lowers Body Weight By Increasing Energy Expenditure

Because both glucagon (Habegger et al., 2013) and T$_3$ (Silva, 2006) have been reported to increase energy expenditure and decrease body fat, we explored the weight-lowering capacity of glucagon/T$_3$ in diet-induced obese (DIO) mice maintained on a high-fat, high-sugar diet (HFHSD). Glucagon/T$_3$ dose-dependently lowered body weight (Figure S3B). At a dose that is sub-threshold for glucagon or T$_3$ to lower body weight, a 10% absolute decrease from baseline was observed after a week of treatment with glucagon/T$_3$ (Figure 4A). At a dose with minimal effects on body weight, glucagon/T$_3$ lowered cholesterol (Figure S3A), thus demonstrating weight-independent effects on plasma lipids. Neither of the other conjugates or co-administration lowered body weight to the same magnitude as glucagon/T$_3$ (Figures S4E and S4F). The loss of body weight caused by glucagon/T$_3$ was due to a loss of fat mass, not lean mass (Figure 4B). Food intake was increased by systemic T$_3$ treatment and co-administration, recapitulating the hyperphagia associated with hyperthyroidism (Kong et al., 2004), yet was not increased by glucagon/T$_3$ (Figures 4C, S4G, and S4H). Despite the difference in energy intake, T$_3$, glucagon/T$_3$, and the physical mixture of glucagon and T$_3$ substantially increased whole-body energy expenditure (Figures 4D, S4I, and S4J). However, the hyperphagia following treatment with T$_3$ compensated for increased energy expenditure, while glucagon/T$_3$ drove a negative energy balance resulting in a loss of body fat. Whereas systemic T$_3$ significantly increased ambulatory activity and rectal temperature, which paralleled the observed increase in energy expenditure, the conjugate did not cause an increase in either measure (Figures 4E and 4F). This again is decidedly different from their co-administration (Figures S4K and S4L). Glucagon/T$_3$ decreased the respiratory exchange ratio (RER) without altering food intake (Figure 4G), demonstrating that glucagon/T$_3$ shifted nutrient partitioning to promote fat utilization. Co-administration as well as the two thyromimetics also decreased RER (Figures S4M and S4N), but co-administration concomitantly increased food intake.

Similar to the lack of cholesterol and triglyceride lowering effects observed in *Gcgr*$^{-/-}$ mice, the effects of glucagon/T$_3$ to lower body weight (Figure 4H), enhance energy expenditure (Figure 4I), and promote fat utilization (Figure 4J) were likewise
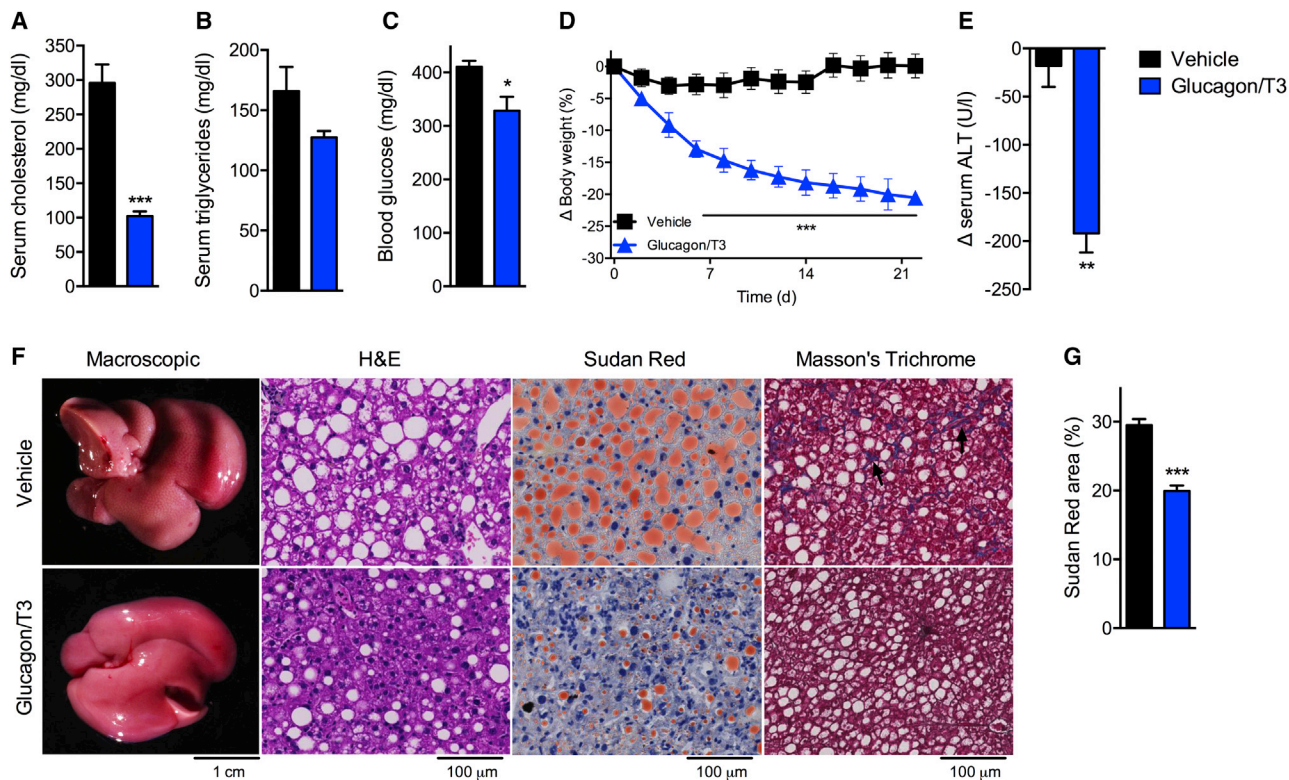
Figure 3. Glucagon/T$_3$ Improves Symptoms Associated with NAFLD-Induced NASH

Effects on serum levels of (A) cholesterol and (B) triglycerides, (C) ad libitum fed blood glucose, (D) body weight change, (E) change in serum ALT levels, (F) liver histology and diagnostic staining, and (G) Sudan red-positive area of liver sections from CD-HFD-fed male C57Bl6j mice following daily s.c. injections of vehicle (black) or glucagon/T$_3$ (blue) at a dose of 100 nmol kg^{-1} for 21 days (n = 5). Arrows indicate positive trichrome staining of collagen indicative of fibrosis.

*p < 0.05 and ***p < 0.001 comparing effects following compound injections to vehicle injections. All data are presented as mean ± SEM.

See also Table S1.

---

absent in *Gcgr*$^{-/-}$ mice. Here, in the absence of the GcgR cellular gateway, the covalent attachment of T$_3$ to glucagon inactivates thyroid hormone pharmacology and enhanced metabolic efficacy is not observed.

Glucagon/T$_3$ Induces the Browning of Inguinal White Fat

Based on the indirect calorimetry results, the low level of trafficking to inguinal white adipose tissue (iWAT) (Figure S5D) and the presence of GcgR in white adipose tissue (WAT) (Burcelin et al., 1995), albeit at a level that is fractional compared to the liver (Figures S5E), we next tested the in vivo effects of glucagon/T$_3$ on iWAT and thermogenesis. Although the levels of T$_3$ residing in iWAT are below the limits of detection in a basal state, chronic treatment with glucagon/T$_3$ delivered a detectable amount of T$_3$ in iWAT, as did treatment with T$_3$ (Figure 5A). The conjugate increased the multilocular nature of iWAT and reduced adipocyte size to a similar extent as systemic T$_3$ whereas glucagon alone had negligible effects at this dose (Figure 5B). Much like T$_3$ itself, glucagon/T$_3$ turned on thermogenic gene programs in iWAT (Figure 5C) and triggered an increase of uncoupling protein-1 (UCP-1) immunoreactivity in iWAT (Figure 5D). However, the effects of glucagon/T$_3$ to induce UCP-1 are of lesser magnitude than T$_3$ itself. Glucagon/T$_3$ had minimal effects

on gene profile changes in brown adipose tissue (BAT) (data not shown), which is consistent with reports of a lack of direct thermogenic effects on BAT by pharmacological glucagon (Dicker et al., 1998) and thyromimetics (Lin et al., 2015).

To test whether the observed iWAT browning and beige fat thermogenesis is dispensable for the effects on body and energy expenditure driven by glucagon/T$_3$, we tested the conjugate in *Ucp1* knockout mice (*Ucp1*$^{-/-}$). The body weight lowering of glucagon/T$_3$ was blunted, but not completely silenced in *Ucp1*$^{-/-}$ mice compared to wild-type controls (Figure 5E). Likewise, the magnitude of the shift in RER (Figure 5F) and the increase in energy expenditure (Figure 5G) induced by glucagon/T$_3$ were diminished in *Ucp1*$^{-/-}$ mice compared to wild-type mice. This attenuation shows UCP1-dependency yet indicates that other mechanisms contribute additional benefits.

Hepatic action of glucagon/T$_3$ results in an increase in FGF21, which may convey some of benefits on energy metabolism. To determine the FGF21 contribution, we tested the glucagon/T$_3$ conjugate in *Ffg21*$^{-/-}$ mice. Like *Ucp1*$^{-/-}$ mice, the body weight lowering potency of glucagon/T$_3$ was diminished, but not completely lost in *Fgf21*$^{-/-}$ mice relative to wild-type controls (Figure 5H). The decreased RER appears magnified in *Fgf21*$^{-/-}$ mice compared to wild-type controls (Figure 5I) yet the increase
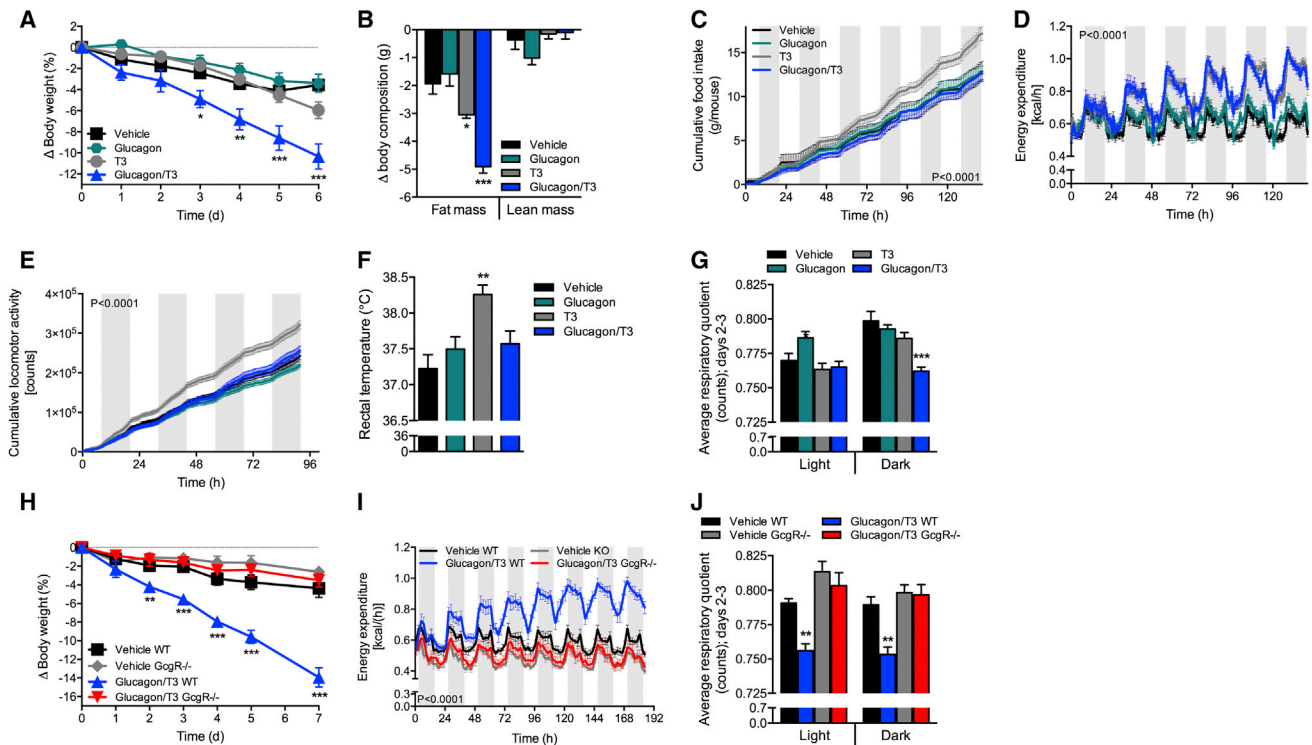
Figure 4. Glucagon/T₃ Increases Energy Expenditure and Lowers Body Weight in DIO Mice

(A–G) Effects on (A) body weight change, (B) body composition, (C) cumulative food intake, (D) longitudinal energy expenditure, (E) cumulative locomotor activity, (F) rectal temperature, and (G) average diurnal RER from HFHSD-fed male C57Bl6j mice following daily s.c. injections of vehicle (black), a glucagon analog (teal), T₃ (gray), or glucagon/T₃ (blue) at a dose of 100 nmol kg^{-1} for 7 days (n = 8).

(H–J) Effects on (H) body weight change, (I) longitudinal energy expenditure, and (J) average diurnal RER from HFHSD-fed global GcgR$^{-/-}$ male mice or wild-type controls following daily s.c. injections of vehicle or glucagon/T₃ at a dose of 100 nmol kg^{-1} for 7 days (n = 7–9).

*p < 0.05, **p < 0.01, and ***p < 0.001 comparing effects following compound injections to vehicle injections within comparable genotypes. All data are presented as mean ± SEM.

See also Figures S3 and S4.

in energy expenditure observed in wild-type mice is not as pronounced in *Fgf21*$^{-/-}$ mice (Figure 5J).

Concurrent T₃ Activity Neutralizes the Diabetogenic Action Profile of Glucagon

The therapeutic utility glucagon for chronically treating obesity is compromised by its promotion of hepatic glucose production. Therefore, we tested whether targeted T₃ action could counteract the adverse effects of glucagon on glycemic control in DIO mice. The addition of the T₃ moiety to glucagon dampened acute hyperglycemia (Figure 6A), improved acute glucose tolerance (Figure 6B), and dose-dependently prevented the development of glucose intolerance or hyperglycemia after chronic treatment (Figures 6C and S3C), which were evident with glucagon treatment alone. Chronic treatment with the ancillary glucagon and T₃ combination therapies all resulted in improved glycemia relative to vehicle controls as well, yet glucagon/T₃ outperformed all of these treatments (Figures S4O and S4P). The improved glucose tolerance after chronic treatment with glucagon/T₃ was lost in *Gcgr*$^{-/-}$ mice, liver-specific *Thrb*$^{-/-}$ mice, and *Fgf21*$^{-/-}$ mice (Figures S6A–S6C) yet preserved in *Ucp1*$^{-/-}$ mice (Figure S6D). Glucagon/T₃ improved in-

sulin sensitivity (Figure 6D) and lowered plasma levels of insulin (Figure 6E). We used a pyruvate tolerance test as an indirect measure of hepatic glucose output. Glucagon worsened pyruvate tolerance whereas T₃ substantially improved the effect. The attached T₃ moiety on glucagon/T₃ was capable of completely offsetting the gluconeogenic effects of glucagon (Figure 6F). Furthermore, the attached T₃ moiety, but not as a co-administration, prevented the glucagon-mediated increase in RER, thus limiting the shift to more carbohydrate utilization that is evident with the glucagon alone (Figures 6G and S4Q). This appears to be a direct result of the incorporated T₃ action to lessen the surge in hepatic glucose production combined with increased fatty acid utilization induced by the glucagon component, as evident by the acute decrease in circulating free fatty acids induced by glucagon alone and glucagon/T₃ (Figure 6H).

Both gluconeogenic gene programs and glycolytic gene programs were increased by glucagon/T₃ in the liver (Figure 6I). These opposing forces suggest glucose futile cycling is involved. The gluconeogenic actions of glucagon are partly governed by engaging the peroxisome proliferator receptor gamma coactivator-1 (PGC-1) axis (Herzig et al., 2001), acting
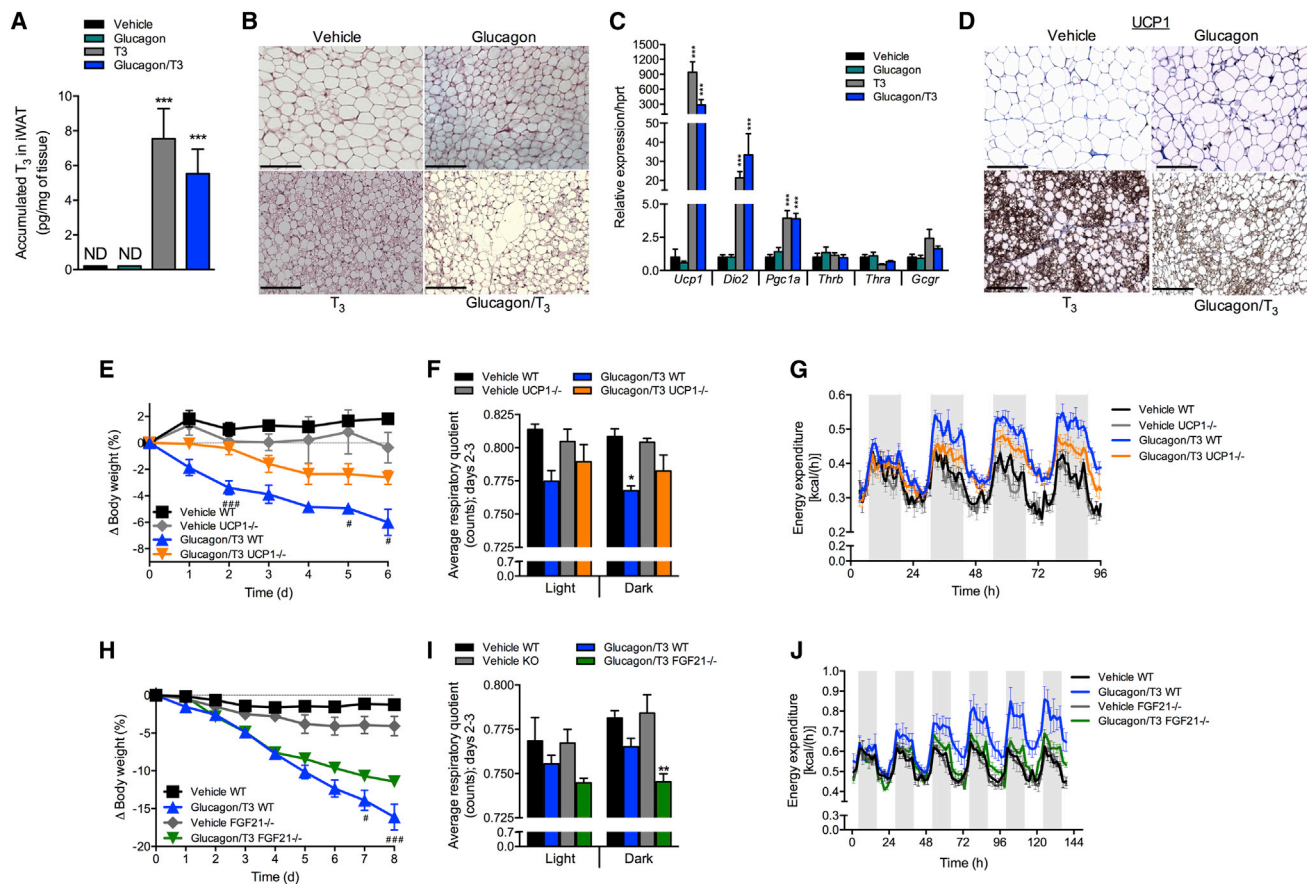
Figure 5. Glucagon/T₃ Induces Browning of iWAT and Full Weight-Lowering Efficacy Depends on UCP-1- and FGF21-Mediated Thermogenesis

(A–D) Effects on (A) levels of iWAT T₃, (B) iWAT H&E staining, (C) iWAT mRNA expression of select targets, and (D) UCP-1 immunoreactivity in iWAT from HFHCD-fed male C57Bl6j mice following daily s.c. injections of vehicle, a glucagon analog, T₃, or glucagon/T₃ at a dose of 100 nmol kg^{-1} for 14 days (n = 8).

(E–G) Effects on (E) body weight change, (F) average diurnal RER, and (G) longitudinal energy expenditure from HFHSD-fed global $Ucp1^{-/-}$ male mice or wild-type controls maintained at 30°C following daily s.c. injections of vehicle or glucagon/T₃ at a dose of 100 nmol kg^{-1} for 7 days (n = 4–7).

(H–J) Effects on (H) body weight change, (I) average diurnal RER, and (J) longitudinal energy expenditure from HFHSD-fed global $Fgf21^{-/-}$ male mice or wild-type controls following daily s.c. injections of vehicle or glucagon/T₃ at a dose of 100 nmol kg^{-1} for 7 days (n = 4–8).

*p < 0.05, **p < 0.01, and ***p < 0.001 comparing effects following compound injections to vehicle injections. #p < 0.05, ##p < 0.01, and ###p < 0.001 comparing effects between genotypes following compound injections. All data are presented as mean ± SEM.

See also Figures S3 and S4.

to increase PGC-1α levels and repress PGC-1β levels. Herein, we show that concurrent T₃ action within the glucagon/T₃ conjugate mitigates the glucagon-mediated increase in *Pgc1a* mRNA levels and simultaneously prevents the glucagon-mediated suppression of *Pgc1b* mRNA levels (Figure 6J). Both glucagon and glucagon/T₃ increase the phosphorylation of protein kinase A (PKA) in livers of acutely treated mice to a comparable level whereas T₃ alone has no influence (Figure 6K). CREB is intermediary to PKA and the PGC-1 axis and governs the transcription of *Pgc1a*, the PGC-1 member responsible for promoting gluconeogenic machinery (Herzig et al., 2001). Interestingly, we see that glucagon-mediated phosphorylation of CREB was reduced with glucagon/T₃ as well as with co-administration compared to glucagon alone (Figures 6K and S6E). This indicates that concomitant T₃ action blunts distal glucagon signaling and aligns with the dampened *Pgc1a* mRNA levels,

whereas proximal glucagon signaling is unaltered by the presence of T₃.

Glucagon-Mediated T₃ Delivery Prevents Cardiovascular and Bone Thyrotoxicity

The therapeutic use of T₃ in obesity is undermined by deleterious effects on the cardiovascular system. Because of these concerns, as well as a low level of heart targeting that was detected by glucagon-mediated delivery (Figure S5D), we assessed the impact of glucagon/T₃ on cardiac hypertrophy in DIO mice after chronic treatment (all echocardiography parameters in Table S2). High-dose T₃ mono-therapy reduced heart rate (Figure 7A) and increased respiration rate (Figure 7B), whereas glucagon/T₃ had no effect on either parameter. At a lower dose that still provides lipid improvements without body weight improvements (Figures S3A and S3B), T₃ elevated heart rate (Figure S7A) and
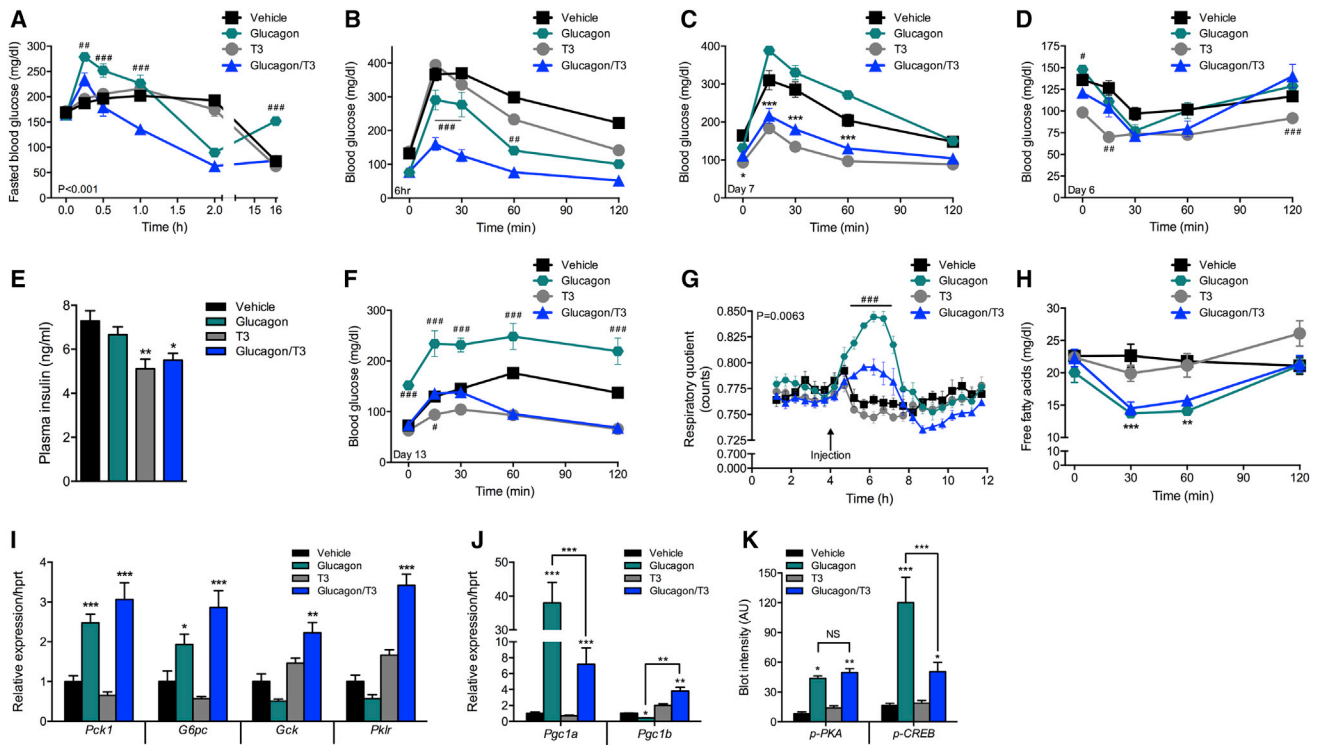
Figure 6. The T_3 Action of Glucagon/T_3 Overpowers the Hyperglycemic Effects of Glucagon

(A) Effects on 6-hr fasted blood glucose through 120 min and ad libitum-fed blood glucose at 16 hr from HFHSD-fed male C57Bl6j mice following a single s.c. injection of vehicle (black), a glucagon analog (teal), T_3 (gray), or glucagon/T_3 (blue) at a dose of 100 nmol kg^{-1} (n = 8).

(B–F) Effects on (B) acute (6 hr after therapy) and (C) chronic (after 7 days of therapy) intraperitoneal glucose tolerance (1.5 g kg^{-1}), (D) intraperitoneal insulin tolerance (0.75 IU kg^{-1}), (E) plasma levels of insulin, and (F) intraperitoneal pyruvate tolerance (1.5 g kg^{-1}) at the indicated days from HFHSD-fed male C57Bl6j mice following daily s.c. injections of vehicle (black), a glucagon analog (teal), T_3 (gray), or glucagon/T_3 (blue) at a dose of 100 nmol kg^{-1} (n = 8).

(G) Acute effects on RER from HFHSD-fed male C57Bl6j mice immediately following a s.c. injection of vehicle (black), a glucagon analog (teal), T_3 (gray), or glucagon/T_3 (blue) at a dose of 100 nmol kg^{-1} (n = 8).

(H) Effects on plasma levels of free fatty acids from HFHSD-fed male C57Bl6j mice following a single s.c. injection of vehicle (black), a glucagon analog (teal), T_3 (gray), or glucagon/T_3 (blue) at a dose of 100 nmol kg^{-1} (n = 8).

(I and J) Effects on hepatic mRNA expression of (I) select targets indicative of glucose metabolism and (J) the PGC-1 axis from HFHCD-fed male C57Bl6j mice following daily s.c. injections of vehicle (black), a glucagon analog (teal), T_3 (gray), or glucagon/T_3 (blue) at a dose of 100 nmol kg^{-1} for 14 days (n = 8).

(K) Acute effects on levels of phosphorylated PKA and CREB normalized to GAPDH in livers of lean C57Bl6j mice 15 min following a s.c. injection of vehicle (black), a glucagon analog (teal), T_3 (gray), or glucagon/T_3 (blue) at a dose of 100 nmol kg^{-1} (n = 8).

*$p < 0.05$, **$p < 0.01$, and ***$p < 0.001$ comparing effects following compound injections to vehicle injections. #$p < 0.05$, ##$p < 0.01$, and ###$p < 0.001$ comparing effects between glucagon and glucagon/T_3 injections. All data are presented as mean ± SEM.

See also Figures S3, S4, and S6.

increased heart size (Figure S7B) relative to vehicle controls whereas glucagon/T_3 did not impact either measure. T_3 also reduced fraction shortening (Figure 7C) and ejection fraction (Figure 7D). Once again, the conjugate had no apparent effect on cardiac performance (Figures 7C and 7D). T_3 mono-therapy, but not glucagon/T_3, increased the tibia length-corrected heart weight (Figure 7E). The cardiac hypertrophy observed with T_3 co-incides with increased diastolic and systolic left ventricular wall thickness (Figures 7F and 7G), and planar cross-sectional area (Figure 7H), pathological processes that do not occur with glucagon/T_3 treatment. T_3 increased the expression of T_3-sensitive genes (Figure S7C) and hypertrophic gene markers (Figure S7D) in the whole heart, which were not regulated by glucagon/T_3. T_3-treated mice displayed marked histopathological features of thyrotoxic cardiomyopathy, including larger

cardiomyocytes, increased fat deposition, and infiltration of fibroblast and inflammatory cell into interstitial tissue (Figure 7H). Marked cell death was detectable in the hearts of T_3-treated mice, including both single cell necrosis as well as larger infarction. None of these manifestations of thyrotoxicity were detectable following treatment with the glucagon/T_3 conjugate at the same molar dose.

We also examined the effects of the conjugate on hypothalamic-pituitary-thyroid (HPT) feedback regulation. T_3 but not the conjugate increased circulating levels of T_3 (Figure S7E). Circulating levels of thyroxine were further reduced by T_3 than by glucagon/T_3 (Figure S7F). Despite these changes, serum levels of thyroid-stimulating hormone (TSH) (Figure S7G) and hypothalamic expression of thyroid releasing hormone (*Trh*) (Figure S7H) were not affected by any treatment in this setting.
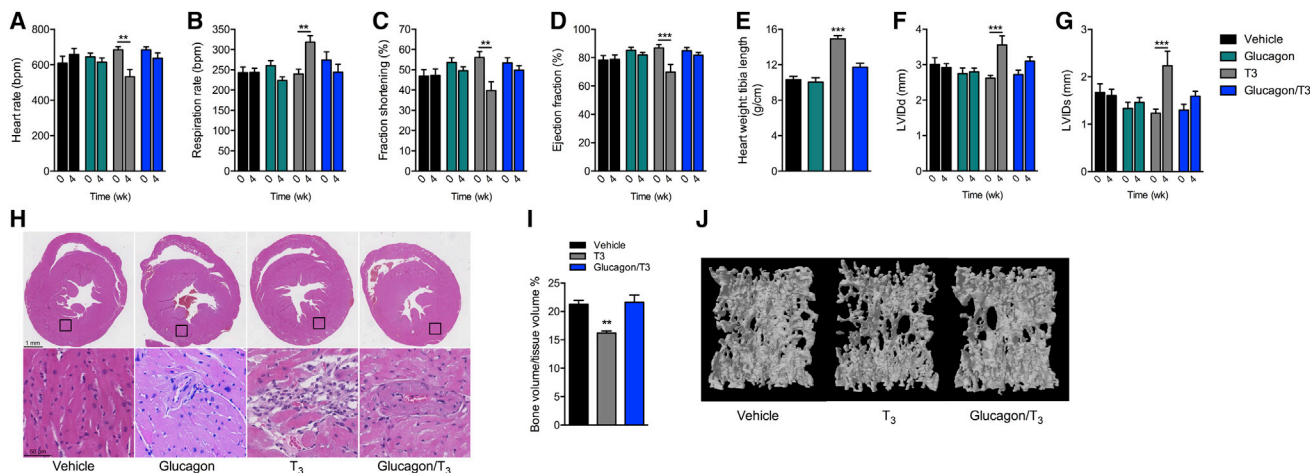
Figure 7. Glucagon/T$_3$ Is Devoid of Adverse Effects on Cardiac Function and Bone Health

(A–H) Effects on (A) heart rate, (B) respiration rate, (C) fraction shortening, (D) ejection fraction, (E) heart weight to tibia length ratio, left ventricular internal diameter at the end of (F) diastole and (G) systole, and (H) H&E staining of heart cross sections from HFHSD-fed male C57Bl6j mice following daily s.c. injections of vehicle (black), a glucagon analog (teal), T$_3$ (gray), or glucagon/T$_3$ (blue) at a dose of 100 nmol kg^{-1} (n = 8) for 28 days.

(I and J) Effects on (I) bone volume and (J) representative 3D reconstructions of lumbar vertebrae L5 from lean C57Bl6j mice following a s.c. injection of vehicle (black), a glucagon analog (teal), T$_3$ (gray), or glucagon/T$_3$ (blue) at a dose of 25 nmol kg^{-1} for 14 days (n = 8).

*p < 0.05, **p < 0.01, and ***p < 0.001 comparing effects following compound injections to vehicle injections. All data are presented as mean ± SEM.

See also Figure S7 and Table S2.

Because some thyromimetics can negatively impact bone metabolism, we examined the effects on bone density in lean mice following chronic treatment with T$_3$ and glucagon/T$_3$. At a dose of glucagon/T$_3$ that achieves both body weight lowering and lipid lowering advantages (Figures S3A–S3C), glucagon/T$_3$ did not affect bone volume (Figures 7I and 7J) or markers of bone turnover (Figures S7I and S7J). T$_3$, however, substantially reduced bone volume (Figures 7I and 7J). Like measures on cardiac performance and HPT regulation, the diminished of effects on bone turnover observed with glucagon/T$_3$ demonstrates that we have improved the therapeutic window of T$_3$ through its covalent attachment to glucagon and the subsequent preferential delivery to the liver.

DISCUSSION

The beneficial functions of thyroid hormone on systemic metabolism are largely aligned with chronic actions of glucagon on lipid metabolism and body weight. Here, we show that by using glucagon as a targeting ligand, unbiased thyroid hormone action can be selectively guided to the liver and adipose depots, where synergistic benefits on lipid metabolism and adiposity are unleashed. Importantly, we can uncouple these metabolic benefits from deleterious effects on the cardiovascular system and bone turnover that would otherwise arise from systemic thyroid hormone action. Furthermore, the liver-specific effects of thyroid hormone action counteract the diabetogenic effects of glucagon action, completing mutual cancellation of the inherent limitations of each hormone.

Individual TR and GcgR activation in the liver favorably influence lipid homeostasis by both overlapping and independent mechanisms (Habegger et al., 2010; Sinha et al., 2014). We

show that glucagon and T$_3$ signaling pathways converge to reverse hypercholesterolemia through pleotropic mechanisms. The observed synergism and reciprocal regulation of certain gene targets offer clues to molecular underpinnings that could be mediating many of the responses. Glucagon/T$_3$ increased the expression of *Ldlr*, demonstrating that conventional cholesterol uptake mechanisms are being engaged and aligned with classical actions of glucagon on hepatic cholesterol metabolism. However, the preserved efficacy in *Ldlr$^{-/-}$* mice suggests nontraditional mechanisms for cholesterol reabsorption by the liver are contributing to the observed effects, which overlaps with studies of T$_3$ in *Ldlr$^{-/-}$* mice (Lin et al., 2012). The fact that we find less cholesterol deposited in the liver yet increased markers of conventional and reverse cholesterol uptake suggests that we are stimulating localized conversion to bile acids. Additionally, coordinated glucagon and T$_3$ signaling results in increased induction of *fgf21* in the liver and elevated FGF21 presence in circulation, which itself has many pharmacological benefits on lipid and energy metabolism (Kharitonenkov and Adams, 2013). Glucagon and T$_3$ independently complement FGF21 action and many of their actions on systemic metabolism require FGF21 (Habegger et al., 2013; Domouzoglou et al., 2014).

Glucagon and thyroid hormone have individually been shown to have beneficial effects on hepatic triglyceride metabolism (Sinha et al., 2012; Penhos et al., 1966). We show that glucagon-mediated targeting of T$_3$ effectively removes fat deposition in the liver more potently than either agent alone without worsening insulin sensitivity or promoting hyperthermia in mice fed obesogenic diets. In addition, glucagon/T$_3$ therapy improved liver function, steatosis, and the mild fibrosis evident in mice fed a diet prone to inducing NASH. These effects are analogous to a

liver-targeted chemical uncoupler that showed beneficial results in rodent models of NAFLD (Perry et al., 2013). The secondary effects of glucagon/T_3 on adipose tissue and the associated modest weight-lowering efficacy will only further support alleviating disease symptoms of NASH, as our preliminary data demonstrate. We speculate that a glucagon/T_3 co-agonist could have a future application in NASH, a disease for which an effective treatment is currently lacking (Schwenger and Allard, 2014).

Coordinated thyroid hormone action at the liver is appropriately positioned to counteract the hyperglycemic effects of glucagon by a mechanism different from what we achieved previously with integrated GLP-1 action (Day et al., 2009; Finan et al., 2015). Much of the glucagon-opposing actions of GLP-1 on glycemia are mediated through effects in other tissues, notably in the pancreas and central nervous system. Here, we direct T_3 as a specific pharmacological agent to the liver in order to directly counteract the localized glucose production induced by glucagon. The addition of thyroid hormone action lessens the acute rise in blood glucose that is otherwise seen with unopposed glucagon administration and improves glucose utilization after glucose, insulin, and pyruvate challenges that are ordinarily deteriorated after chronic glucagon treatment. These disparate effects on hepatic glucose metabolism appear to be partly governed by influencing the PGC-1 axis through differential downstream signaling from GcgR, which may also contribute to the observed benefits on hepatic lipid oxidation as our transcriptional data suggest (Finck and Kelly, 2006; Lin et al., 2005).

The weight loss following glucagon/T_3 therapy is due to increased energy expenditure, some of which is mediated via lipolytic mechanisms and the recruitment of thermogenesis-capable adipocytes in iWAT. Both glucagon and T_3 have individually been reported to increase UCP1 activity in vivo (Bianco and Silva, 1987; Billington et al., 1991), and here we demonstrate that the conjugate induces browning of iWAT analogous to thyromimetics (Lin et al., 2015). Our data indicates that a percentage of the T_3 that normally accesses iWAT following systemic T_3 administration is being targeted to iWAT by glucagon/T_3. The blunted weight-lowering effect of the conjugate in $Ucp1^{-/-}$ mice underscores that the increased energy expenditure induced by glucagon/T_3 is at least in part a consequence of UCP1-dependent thermogenic mechanisms without concomitant pyrexia. In relation to a permissible effect through FGF21, the effects of FGF21 on brown fat thermogenesis and body weight do not rely on UCP-1 (Samms et al., 2015; Véniant et al., 2015), whereas here we show that glucagon/T_3 partially relies on UCP-1 for a maximal effect on body weight. Likewise, we show that the thermogenic effects of glucagon/T_3 are mediated through FGF21, and the body weight-lowering benefit is partially dependent on FGF21 function. This demonstrates that other body weight-lowering mechanisms independent from FGF21 action are being engaged, and we speculate that macronutrient futile cycling may be facilitating part of the effects.

Chronic hyperthyroidism evolves into cardiac malfunctions such as arrhythmias that eventually progress to irreversible, serious heart damage. This in itself has limited the therapeutic utility of thyroid hormones for treating chronic diseases not associated with deficient thyroid status and is why thyromimetics were specifically engineered to activate TRβ isoforms that are not present in the cardiovascular system. We show that glucagon-mediated targeting limits cardiomyocyte entry and spares the cardiovascular system from direct thyroid hormone action. Chronic therapy with glucagon/T_3 is not associated with cardiac hypertrophy, altered ventricular function, or cardiomyocyte necrosis, all of which were observed with an equimolar treatment with T_3 and resulted in severely impaired cardiac performance. Conversely, glucagon/T_3 causes mobilization and utilization of triglycerides and cholesterol and prevents the accumulation of atherosclerotic plaques in the aortic root, all of which are vital to reduce CHD risk. Because FGF21 has been shown to protect from cardiac hypertrophy (Planavila et al., 2013), it is plausible that the observed FGF21 induction contributes to the cardiac profile of glucagon/T_3. Clinical testing of first generation thyromimetics revealed an unexpected finding of increased bone turnover (Ladenson et al., 2010) and deleterious effects on bone cartilage in dogs (Sjouke et al., 2014). Although we have shown that glucagon/T_3 does not impair bone mineral density at doses where T_3 induces bone loss, we have to be mindful of these overlapping links of T_3 and FG21 to bone metabolism (Wei et al., 2012; Wang et al., 2015) as we continue development of glucagon/T_3.

Glucagon-mediated targeting offers an alternative to designing isoform-selective thyromimetics, which has proven difficult due to structural similarities in the binding pocket of TR isoforms (Wagner et al., 2001). Unlike other strategies for hepatic targeting of thyroid hormone action (Kelly et al., 2014; Taub et al., 2013), glucagon-mediated targeting mimics an embellished Trojan Horse approach. The engineered co-agonism allows for coordinated polypharmacology arising from T_3 and the inherent activity of the glucagon carrier, which complements TR signaling patterns and importantly directs the T_3 payload to preferential sites of action. Secondary actions in adipose depots contribute weight-lowering mechanisms that enrich the therapeutic utility of glucagon/T_3 co-agonists. Perhaps the most compelling data are that synergistic signaling improved the otherwise narrow therapeutic index of T_3. The next step in translational development should focus on higher mammals that more closely resemble human pathology. The quantification of relative efficacy and more in-depth safety profiling will guide timing to subsequent human study and the need for further chemical optimization. Cumulatively, the data we present support the potential therapeutic utility of pairing glucagon and thyroid hormones to a single molecule that might constitute a suitably efficacious therapy for the chronic treatment of the constellation of disorders that constitute the metabolic syndrome, including obesity, fatty liver disease, type 2 diabetes, and atherosclerosis.

STAR★METHODS

Detailed methods are provided in the online version of this paper and include the following:

- KEY RESOURCES TABLE
- CONTACT FOR REAGENT AND RESOURCE SHARING
- EXPERIMENTAL MODEL AND SUBJECT DETAILS
  - Wild-Type Mice for Pharmacology Studies
  - Genetically-Modified Mouse Lines

- **METHOD DETAILS**
  - Peptide Synthesis
  - Synthesis of Glucagon/T$_3$ Conjugate
  - Synthesis of Glucagon/iT$_3$ Conjugate
  - Synthesis of Glucagon/rT$_3$ Conjugate
  - Human Glucagon Receptor Activation
  - TR Transcriptional Activity
  - Plasma Stability
  - RNA sequencing
  - Pathway Enrichment
  - Rodent Pharmacological and Metabolism Studies
  - Body Composition Measurements
  - Indirect Calorimetry
  - Blood Parameters
  - Histopathology
  - In Vivo Biodistribution Imaging
  - Echocardiography
  - Rectal Body Temperature
  - Atherosclerotic Plaque Assessment
  - Immunohistochemistry For UCP1
  - Bone Density Measurements
  - Quantification of Accumulated T$_3$ In Liver and iWAT
  - Gene Expression Analysis
- **QUANTIFICATION AND STATISTICAL ANALYSIS**
- **DATA AND SOFTWARE AVAILABILITY**
  - Data Resources

SUPPLEMENTAL INFORMATION

Supplemental Information includes seven figures and three tables and can be found with this article online at http://dx.doi.org/10.1016/j.cell.2016.09.014.

AUTHOR CONTRIBUTIONS

B.F. co-conceptualized the project, designed and performed in vitro, in vivo, and ex vivo rodent experiments, synthesized and characterized compounds, analyzed and interpreted data, and co-wrote the manuscript. C.C. designed and performed in vitro, in vivo, and ex vivo rodent experiments, analyzed and interpreted data, and co-wrote the manuscript. Z.Z. and B.Y. designed, synthesized, and characterized compounds, and performed in vitro experiments. K.S. designed, performed, and interpreted biodistribution and imaging studies. L.M., K.F., M.A.S.-G., M.K., S.B., and S.J. performed in vitro, in vivo, and ex vivo rodent experiments. K.G., F.F., and D.P.-T. generated loss of function mouse models and interpreted data. K.M. interpreted measures for cardiovascular function. F.N. interpreted histopathological cardiac data. P.L. and J.T. performed and interpreted bone turnover measures. M.M., A.W., M.E.H., and M.H. performed and interpreted NAFLD-induced NASH studies. K.G., D.L., and F.F. performed and interpreted RNA-seq data. V.G. and H.B. supervised and interpreted in vitro experiments. Y.D. and C.W. helped design and interpreted data on atherosclerosis. K.M.H. designed and interpreted loss-of-function studies. M.D.A. and K.-W.S. performed and interpreted ex vivo quantification of thyroid hormones in tissues. M.J. and M.K. interpreted in vivo and in vitro experiments on adipocyte metabolism. F.L. assisted in design of fluorescently labeled conjugates. J.K. provided expert opinion on thyroid hormone function and appropriate methods for assessing thyroid hormone action. J.R., H.F., V.G.-D., and M.H.d.A. interpreted data. S.M.H helped design in vivo experiments, analyzed and interpreted atherosclerosis and lipid homeostasis data, and supervised experiments. R.D.D. and M.H.T. co-conceptualized the project and interpreted all studies. T.D.M. co-conceptualized the project, interpreted all data, supervised all studies, and co-wrote the manuscript with B.F. and C.C.

REFERENCES

Baxter, J.D., and Webb, P. (2009). Thyroid hormone mimetics: potential applications in atherosclerosis, obesity and type 2 diabetes. Nat. Rev. Drug Discov. 8, 308–320.

Bianco, A.C., and Silva, J.E. (1987). Intracellular conversion of thyroxine to triiodothyronine is required for the optimal thermogenic function of brown adipose tissue. J. Clin. Invest. 79, 295–300.

Billington, C.J., Briggs, J.E., Link, J.G., and Levine, A.S. (1991). Glucagon in physiological concentrations stimulates brown fat thermogenesis in vivo. Am. J. Physiol. 261, R501–R507.

Billon, C., Canaple, L., Fleury, S., Deloire, A., Beylot, M., Dombrowicz, D., Del Carmine, P., Samarut, J., and Gauthier, K. (2014). TRalpha protects against atherosclerosis in male mice: identification of a novel anti-inflammatory property for TRalpha in mice. Endocrinology 155, 2735–2745.

Burcelin, R., Li, J., and Charron, M.J. (1995). Cloning and sequence analysis of the murine glucagon receptor-encoding gene. Gene 164, 305–310.

Day, J.W., Ottaway, N., Patterson, J.T., Gelfanov, V., Smiley, D., Gidda, J., Findeisen, H., Bruemmer, D., Drucker, D.J., Chaudhary, N., et al. (2009). A new

glucagon and GLP-1 co-agonist eliminates obesity in rodents. Nat. Chem. Biol. *5*, 749–757.

Diamond, D.M., and Ravnskov, U. (2015). How statistical deception created the appearance that statins are safe and effective in primary and secondary prevention of cardiovascular disease. Expert Rev. Clin. Pharmacol. *8*, 201–210.

Dicker, A., Zhao, J., Cannon, B., and Nedergaard, J. (1998). Apparent thermogenic effect of injected glucagon is not due to a direct effect on brown fat cells. Am. J. Physiol. *275*, R1674–R1682.

Domouzoglou, E.M., Fisher, F.M., Astapova, I., Fox, E.C., Kharitonenkov, A., Flier, J.S., Hollenberg, A.N., and Maratos-Flier, E. (2014). Fibroblast growth factor 21 and thyroid hormone show mutual regulatory dependency but have independent actions in vivo. Endocrinology *155*, 2031–2040.

Finan, B., Yang, B., Ottaway, N., Stemmer, K., Müller, T.D., Yi, C.X., Habegger, K., Schriever, S.C., García-Cáceres, C., Kabra, D.G., et al. (2012). Targeted estrogen delivery reverses the metabolic syndrome. Nat. Med. *18*, 1847–1856.

Finan, B., Ma, T., Ottaway, N., Müller, T.D., Habegger, K.M., Heppner, K.M., Kirchner, H., Holland, J., Hembree, J., Raver, C., et al. (2013). Unimolecular dual incretins maximize metabolic benefits in rodents, monkeys, and humans. Sci. Transl. Med. *5*, 209ra151.

Finan, B., Yang, B., Ottaway, N., Smiley, D.L., Ma, T., Clemmensen, C., Chabenne, J., Zhang, L., Habegger, K.M., Fischer, K., et al. (2015). A rationally designed monomeric peptide triagonist corrects obesity and diabetes in rodents. Nat. Med. *21*, 27–36.

Finck, B.N., and Kelly, D.P. (2006). PGC-1 coactivators: inducible regulators of energy metabolism in health and disease. J. Clin. Invest. *116*, 615–622.

Fisher, F.M., Estall, J.L., Adams, A.C., Antonellis, P.J., Bina, H.A., Flier, J.S., Kharitonenkov, A., Spiegelman, B.M., and Maratos-Flier, E. (2011). Integrated regulation of hepatic metabolism by fibroblast growth factor (FGF21) in vivo. Endocrinology *152*, 2996–3004.

Gaich, G., Chien, J.Y., Fu, H., Glass, L.C., Deeg, M.A., Holland, W.L., Kharitonenkov, A., Bumol, T., Schilske, H.K., and Moller, D.E. (2013). The effects of LY2405319, an FGF21 analog, in obese human subjects with type 2 diabetes. Cell Metab. *18*, 333–340.

Grover, G.J., Mellström, K., Ye, L., Malm, J., Li, Y.L., Bladh, L.G., Sleph, P.G., Smith, M.A., George, R., Vennström, B., et al. (2003). Selective thyroid hormone receptor-beta activation: a strategy for reduction of weight, cholesterol, and lipoprotein (a) with reduced cardiovascular liability. Proc. Natl. Acad. Sci. USA *100*, 10067–10072.

Habegger, K.M., Heppner, K.M., Geary, N., Bartness, T.J., DiMarchi, R., and Tschöp, M.H. (2010). The metabolic actions of glucagon revisited. Nat. Rev. Endocrinol. *6*, 689–697.

Habegger, K.M., Stemmer, K., Cheng, C., Müller, T.D., Heppner, K.M., Ottaway, N., Holland, J., Hembree, J.L., Smiley, D., Gelfanov, V., et al. (2013). Fibroblast growth factor 21 mediates specific glucagon actions. Diabetes *62*, 1453–1463.

Herzig, S., Long, F., Jhala, U.S., Hedrick, S., Quinn, R., Bauer, A., Rudolph, D., Schutz, G., Yoon, C., Puigserver, P., et al. (2001). CREB regulates hepatic gluconeogenesis through the coactivator PGC-1. Nature *413*, 179–183.

Hotta, Y., Nakamura, H., Konishi, M., Murata, Y., Takagi, H., Matsumura, S., Inoue, K., Fushiki, T., and Itoh, N. (2009). Fibroblast growth factor 21 regulates lipolysis in white adipose tissue but is not required for ketogenesis and triglyceride clearance in liver. Endocrinology *150*, 4625–4633.

Kellendonk, C., Opherk, C., Anlag, K., Schutz, G., and Tronche, F. (2000). Hepatocyte-specific expression of Cre recombinase. Genesis *26*, 151–153.

Kelly, M.J., Pietranico-Cole, S., Larigan, J.D., Haynes, N.E., Reynolds, C.H., Scott, N., Vermeulen, J., Dvorozniak, M., Conde-Knape, K., Huang, K.S., et al. (2014). Discovery of 2-[3,5-dichloro-4-(5-isopropyl-6-oxo-1,6-dihydropyridazin-3-yloxy)phenyl]-3,5-dioxo-2,3,4,5-tetrahydro[1,2,4]triazine-6-carbonitrile (MGL-3196), a highly selective thyroid hormone receptor β agonist

in clinical trials for the treatment of dyslipidemia. J. Med. Chem. *57*, 3912–3923.

Kharitonenkov, A., and Adams, A.C. (2013). Inventing new medicines: the FGF21 story. Mol. Metab. *3*, 221–229.

Kong, W.M., Martin, N.M., Smith, K.L., Gardiner, J.V., Connoley, I.P., Stephens, D.A., Dhillo, W.S., Ghatei, M.A., Small, C.J., and Bloom, S.R. (2004). Triiodothyronine stimulates food intake via the hypothalamic ventromedial nucleus independent of changes in energy expenditure. Endocrinology *145*, 5252–5258.

Ladenson, P.W., McCarren, M., Morkin, E., Edson, R.G., Shih, M.C., Warren, S.R., Barnhill, J.G., Churby, L., Thai, H., O'Brien, T., et al. (2010). Effects of the thyromimetic agent diiodothyropropionic acid on body weight, body mass index, and serum lipoproteins: a pilot prospective, randomized, controlled study. J. Clin. Endocrinol. Metab. *95*, 1349–1354.

Lin, J., Handschin, C., and Spiegelman, B.M. (2005). Metabolic control through the PGC-1 family of transcription coactivators. Cell Metab. *1*, 361–370.

Lin, J.Z., Martagón, A.J., Hsueh, W.A., Baxter, J.D., Gustafsson, J.A., Webb, P., and Phillips, K.J. (2012). Thyroid hormone receptor agonists reduce serum cholesterol independent of the LDL receptor. Endocrinology *153*, 6136–6144.

Lin, J.Z., Martagón, A.J., Cimini, S.L., Gonzalez, D.D., Tinkey, D.W., Biter, A., Baxter, J.D., Webb, P., Gustafsson, J.A., Hartig, S.M., and Phillips, K.J. (2015). Pharmacological activation of thyroid hormone receptors elicits a functional conversion of white to brown fat. Cell Rep. *13*, 1528–1537.

Love, M.I., Huber, W., and Anders, S. (2014). Moderated estimation of fold change and dispersion for RNA-seq data with DESeq2. Genome Biol. *15*, 550.

Morreale de Escobar, G., Pastor, R., Obregon, M.J., and Escobar del Rey, F. (1985). Effects of maternal hypothyroidism on the weight and thyroid hormone content of rat embryonic tissues, before and after onset of fetal thyroid function. Endocrinology *117*, 1890–1900.

Mullur, R., Liu, Y.Y., and Brent, G.A. (2014). Thyroid hormone regulation of metabolism. Physiol. Rev. *94*, 355–382.

Nicholls, S.J., Ballantyne, C.M., Barter, P.J., Chapman, M.J., Erbel, R.M., Libby, P., Raichlen, J.S., Uno, K., Borgman, M., Wolski, K., and Nissen, S.E. (2011). Effect of two intensive statin regimens on progression of coronary disease. N. Engl. J. Med. *365*, 2078–2087.

Ochs, N., Auer, R., Bauer, D.C., Nanchen, D., Gussekloo, J., Cornuz, J., and Rodondi, N. (2008). Meta-analysis: subclinical thyroid dysfunction and the risk for coronary heart disease and mortality. Ann. Intern. Med. *148*, 832–845.

Penhos, J.C., Wu, C.H., Daunas, J., Reitman, M., and Levine, R. (1966). Effect of glucagon on the metabolism of lipids and on urea formation by the perfused rat liver. Diabetes *15*, 740–748.

Perry, R.J., Kim, T., Zhang, X.M., Lee, H.Y., Pesta, D., Popov, V.B., Zhang, D., Rahimi, Y., Jurczak, M.J., Cline, G.W., et al. (2013). Reversal of hypertriglyceridemia, fatty liver disease, and insulin resistance by a liver-targeted mitochondrial uncoupler. Cell Metab. *18*, 740–748.

Planavila, A., Redondo, I., Hondares, E., Vinciguerra, M., Munts, C., Iglesias, R., Gabrielli, L.A., Sitges, M., Giralt, M., van Bilsen, M., and Villarroya, F. (2013). Fibroblast growth factor 21 protects against cardiac hypertrophy in mice. Nat. Commun. *4*, 2019.

Samms, R.J., Smith, D.P., Cheng, C.C., Antonellis, P.P., Perfield, J.W., 2nd, Kharitonenkov, A., Gimeno, R.E., and Adams, A.C. (2015). Discrete aspects of FGF21 in vivo pharmacology do not require UCP1. Cell Rep. *11*, 991–999.

Schwenger, K.J., and Allard, J.P. (2014). Clinical approaches to non-alcoholic fatty liver disease. World J. Gastroenterol. *20*, 1712–1723.

Schwenk, R.W., Baumeier, C., Finan, B., Kluth, O., Brauer, C., Joost, H.G., DiMarchi, R.D., Tschöp, M.H., and Schürmann, A. (2015). GLP-1-oestrogen attenuates hyperphagia and protects from beta cell failure in diabetes-prone New Zealand obese (NZO) mice. Diabetologia *58*, 604–614.

Selmi-Ruby, S., Bouazza, L., Obregon, M.J., Conscience, A., Flamant, F., Samarut, J., Borson-Chazot, F., and Rousset, B. (2014). The targeted inactivation of TRbeta gene in thyroid follicular cells suggests a new mechanism of regulation of thyroid hormone production. Endocrinology *155*, 635–646.

Silva, J.E. (2006). Thermogenic mechanisms and their hormonal regulation. Physiol. Rev. *86*, 435–464.

Sinha, R.A., You, S.H., Zhou, J., Siddique, M.M., Bay, B.H., Zhu, X., Privalsky, M.L., Cheng, S.Y., Stevens, R.D., Summers, S.A., et al. (2012). Thyroid hormone stimulates hepatic lipid catabolism via activation of autophagy. J. Clin. Invest. *122*, 2428–2438.

Sinha, R.A., Singh, B.K., and Yen, P.M. (2014). Thyroid hormone regulation of hepatic lipid and carbohydrate metabolism. Trends Endocrinol. Metab. *25*, 538–545.

Sjouke, B., Langslet, G., Ceska, R., Nicholls, S.J., Nissen, S.E., Öhlander, M., Ladenson, P.W., Olsson, A.G., Hovingh, G.K., and Kastelein, J.J. (2014). Eprotirome in patients with familial hypercholesterolaemia (the AKKA trial): a randomised, double-blind, placebo-controlled phase 3 study. Lancet Diabetes Endocrinol. *2*, 455–463.

Talukdar, S., Zhou, Y., Li, D., Rossulek, M., Dong, J., Somayaji, V., Weng, Y., Clark, R., Lanba, A., Owen, B.M., et al. (2016). A long-acting FGF21 molecule, PF-05231023, decreases body weight and improves lipid profile in non-human primates and type 2 diabetic subjects. Cell Metab. *23*, 427–440.

Taub, R., Chiang, E., Chabot-Blanchet, M., Kelly, M.J., Reeves, R.A., Guertin, M.C., and Tardif, J.C. (2013). Lipid lowering in healthy volunteers treated with multiple doses of MGL-3196, a liver-targeted thyroid hormone receptor-β agonist. Atherosclerosis *230*, 373–380.

Tiano, J.P., Tate, C.R., Yang, B.S., DiMarchi, R., and Mauvais-Jarvis, F. (2015). Effect of targeted estrogen delivery using glucagon-like peptide-1 on insulin secretion, insulin sensitivity and glucose homeostasis. Sci. Rep. *5*, 10211.

Véniant, M.M., Sivits, G., Helmering, J., Komorowski, R., Lee, J., Fan, W., Moyer, C., and Lloyd, D.J. (2015). Pharmacologic effects of FGF21 are independent of the "browning" of white adipose tissue. Cell Metab. *21*, 731–738.

Wagner, R.L., Huber, B.R., Shiau, A.K., Kelly, A., Cunha Lima, S.T., Scanlan, T.S., Apriletti, J.W., Baxter, J.D., West, B.L., and Fletterick, R.J. (2001). Hormone selectivity in thyroid hormone receptors. Mol. Endocrinol. *15*, 398–410.

Wang, X., Wei, W., Krzeszinski, J.Y., Wang, Y., and Wan, Y. (2015). A liver-bone endocrine relay by IGFBP1 promotes osteoclastogenesis and mediates FGF21-induced bone resorption. Cell Metab. *22*, 811–824.

Wei, W., Dutchak, P.A., Wang, X., Ding, X., Wang, X., Bookout, A.L., Goetz, R., Mohammadi, M., Gerard, R.D., Dechow, P.C., et al. (2012). Fibroblast growth factor 21 promotes bone loss by potentiating the effects of peroxisome proliferator-activated receptor γ. Proc. Natl. Acad. Sci. USA *109*, 3143–3148.

Wolf, M.J., Adili, A., Piotrowitz, K., Abdullah, Z., Boege, Y., Stemmer, K., Ringelhan, M., Simonavicius, N., Egger, M., Wohlleber, D., et al. (2014). Metabolic activation of intrahepatic CD8+ T cells and NKT cells causes nonalcoholic steatohepatitis and liver cancer via cross-talk with hepatocytes. Cancer Cell *26*, 549–564.

STAR★METHODS

KEY RESOURCES TABLE

REAGENT or RESOURCE	SOURCE	IDENTIFIER
Antibodies		
Rabbit polyclonal to UCP-1	Abcam	Cat # ab10983; RRID: AB_2241462
Rabbit monoclonal to phospho-PKA substrate (RRXS*/T*)	Cell Signaling	Cat # 9624s; RRID: AB_331817
Rabbit monoclonal to phospho-CREB (Ser133)	Cell Signaling	Cat # 9198s; RRID: AB_390802
Mouse monoclonal to GAPDH	Santa Cruz	Cat # sc365062; RRID: AB_10847862
Chemicals, Peptides, and Recombinant Proteins		
Glucagon analog ("Glucagon")	This paper	N/A
Glucagon/T3	This paper	N/A
Glucagon/iT3	This paper	N/A
Glucagon/rT3	This paper	N/A
Glucagon*/T3	This paper	N/A
VivoTag S750	Perkin Elmer	Cat # NEV11224
Genhance 750	Perkin Elmer	Cat # NEV10177
T3	Sigma Aldrich	Cat # T2877
T3	Chem-Impex Int'l Inc.	Cat # 04468
rT3	Ark Pharm, Inc	Cat # AK117028
GC-1	R & D Systems	Cat # 4554
KB2115	Cayman Chemicals	Cat # 10011054
Critical Commercial Assays		
Total cholesterol	Thermo Fisher	Cat # TR13421
Triglycerides	Thermo Fisher	Cat # TR22421
FGF21 ELISA	Millipore	Cat # EXRMFGF21-26K
ALT / AST	Thermo Fisher	Cat # TR71121 / TR70121
Insulin ELISA	Alpco	N/A
Free fatty acids	Wako	Cat # 999-34691, 999-34791, 999-34891 & 999-35191
Blood urea nitrogen	Abcam	Cat # ab83362
Creatinine	Abcam	Cat # ab65340
Hydroxybutyrate	Wako	Cat# 417-73501 & 413-73601
Triiodothyronine (T3) ELISA	Alpco	Cat # 25-TRIHU-E01
Thyroxine (T4) ELISA	Alpco	Cat # 25-TT4HU-E01
Thyroid stimulating hormone (TSH) ELISA	Alpco	Cat # 25-TSHRT-E01
C-terminal collagen crosslinks (CTX) ELISA	Immuno Diagnostic Systems	Cat # AC-06F1
N-terminal propeptide of type 1 collagen (P1NP) ELISA	Immuno Diagnostic Systems	Cat # AC-33F1
Deposited Data		
RNA-Seq	This paper	GSE: 85793
Experimental Models: Cell Lines		
Human: HEK293 cells	ATCC	Cat # CRL-1573
Human: hGcgR luciferase cells	Day et al., 2009	
Human: HepG2	ATCC	Cat # HB-8065
Experimental Models: Organisms/Strains		
Mouse: DIO: C57bl6j	Jackson Laboratories	N/A
Mouse: Ldlr−/−: B6.129S7-Ldlr[tm1Her]/J	Jackson Laboratories	Strain # 002207

(Continued on next page)

Continued

REAGENT or RESOURCE	SOURCE	IDENTIFIER
Mouse: Gcgr−/−:	This paper	N/A
Mouse: Gcgr$^{flox/flox}$:	This paper	N/A
Mouse: Rosa26-$^{Cre-ERT2}$: Gt(ROSA)26Sor$^{tm1(cre/ERT2)tyj}$	Jackson Laboratories	Strain # 008463
Mouse: Liver-specific Thrb−/−: Alfp-creTRβ$^{flox/flox}$	Billon et al., 2014	N/A
Mouse: Alfp-cre:	Kellendonk et al., 2000 / Lab of Günther Schütz	N/A
Mouse: Thrb$^{flox/flox}$	Selmi-Ruby et al., 2014	N/A
Mouse: Ucp1−/−: B6.129-Ucp1^{tm1Kz}/J	Jackson Laboratories	Strain # 003124
Mouse: Fgf21−/−	Hotta et al., 2009	N/A
Sequence-Based Reagents		
For Taqman primers, see Table S3	Life Technologies	N/A
Software and Algorithms		
Synergistic mRNA expression	This paper	N/A
Other		
HFHSD	Research Diets	Cat # D12331
HFHCD	Research Diets	Cat # D10779B
CD-HFD	Research Diets	Cat # D050110402

CONTACT FOR REAGENT AND RESOURCE SHARING

Further information and requests for reagents may be directed to and will be fullfilled by the corresponding author Richard D. DiMarchi, Indiana University (rdimarch@indiana.edu).

EXPERIMENTAL MODEL AND SUBJECT DETAILS

Wild-Type Mice for Pharmacology Studies

For studies on lipid handling in wild-type mice (Western mice), male C57Bl/6j mice (Jackson Laboratories) were fed a atherogenic Western diet (Research Diets D12079B), which is a high-cholesterol diet (0.21% gm %) with 41% kcal from fat, 43% kcal from carbohydrates, and 17% kcal from protein. For studies on energy metabolism in obese mice (DIO mice), male C57Bl/6j mice (Jackson Laboratories) were fed a diabetogenic diet (Research Diets D12331), which is a high-sucrose diet with 58% kcal from fat 25.5% kcal from carbohydrates, and 16.4% kcal from protein. For studies on NAFLD-induced NASH, male C57Bl/6j mice were fed CD-HFD (Research Diets D050110402) for 6 months prior to initiation of treatments. All dietary challenges began at 8 weeks of age. HFHSD, and HFHCD mice were single- or group-housed on a 12:12-h light-dark cycle at 22°C with free access to food and water. Mice were maintained under these conditions for a minimum of 16 weeks before initiation of pharmacological studies and were between the ages of 6 months to 12 months old. All injections and tests were performed during the light cycle. Compounds were administered in a vehicle of 1% Tween-80 and 1% DMSO and were given by daily subcutaneous (s.c.) injections at the indicated doses at a volume of 5 μl per g body weight. Mice were randomized and evenly distributed to test groups according to body weight and body composition. If ex vivo molecular biology/histology/biochemistry analyses were performed, the entire group of mice for each treatment was analyzed and scored in a blinded fashion.

Genetically-Modified Mouse Lines

All rodent studies were approved by and performed according to the guidelines of the Institutional Animal Care and Use Committee of the Helmholtz Center Munich, University of Cincinnati, Universite de Lyon, and in accordance with guidelines of the Association for the Assessment and Accreditation of Laboratory and Animal Care (AAALAC # Unit Number: 001057) and appropriate federal, state and local guidelines, respectively.

Liver-specific *Thrb*$^{−/−}$ mice were generated by crossing *Thrb*$^{flox/flox}$ mice with *Alfp*-Cre mice. *Thrb*$^{flox/flox}$; Cre negative littermates were used as wild-type controls. Mice were maintained on the HFHCD for 8 weeks prior to initiation of treatment. A follow-up study was conducted 4 weeks after the start of the first arm to confirm the effects. The data presented is a compilation of the two independent studies.

Inducible, global *Gcgr*$^{−/−}$ mice were generated by crossing *Gcgr*$^{flox/flox}$ mice with *Rosa26*-$^{Cre-ERT2}$ (tamoxifen-inducible) mice. Design and construction of the Gcgr targeting vector and the subsequent steps to generate mice heterozygous of *Gcgr*$^{flox/+}$ were performed by the Gene Targeted Mouse Service Core at the University of Cincinnati. Briefly, the vector was designed to "flox" exons

4-10 of the *Gcgr* gene, with the neomycin resistant gene and one loxP site being inserted in the intron upstream of exon 4 and the other loxP site in the intron downstream of exon 10. The "floxed" region and the two homologous arms, 3.4 kb and 2.5 kb respectively, were PCR-amplified from mouse genomic DNA and cloned into the vector. The construct was sequenced and then electroporated into mouse ES cells derived from a C57Bl6 strain, and the resulting cells were subject to drug selection on media containing G418. Drug resistant clones were initially screened by PCR and further confirmed by Southern blot analysis. Correctly targeted ES cell clones were injected into albino blastocysts to generate chimeras, which were then bred with C57Bl6 female mice to obtain ES cell-derived offspring as determined by the presence of black coat color. Black mice were further analyzed by PCR for transmission of targeted *Gcgr* gene. The neomycin cassette was deleted by breeding with mice carrying "Flip" recombinase. *Gcgr*$^{flox/+}$ mice lacking the neomycin cassette and Flip allele were selected by subsequent breeding to *wild-type* C57Bl6 mice. The mice were backcrossed to C57Bl6 background for 5 generations and the crossed with *Rosa26*-$^{Cre-ERT2}$ mice (Gt(ROSA)26Sor$^{tm1(cre/ERT2)Tyj}$), obtained from the The Jackson Laboratory (Stock number #008463).

Gcgr$^{flox/flox}$; *Rosa26*-$^{Cre-ERT2}$ mice were maintained on the HFHSD for 12 weeks prior to induction of knockdown via twice daily interaperitoneal injections with tamoxifen (1 mg in 100 µl) for 5 consecutive days. Mice that received oil injections were used as *wild-type* controls. Treatment with compounds were initiated after 2 weeks of washout and recovery following the last tamoxifen injection.

Global *Ldlr*$^{-/-}$ mice and *wild-type* littermates were purchased from Jackson laboratories and were maintained on the HFHCD for 12 weeks prior to treatment initiation. Global *Ucp1*$^{-/-}$ mice and *wild-type* littermates were bred in house, housed at 30°C, and maintained on a HFHSD for 12 weeks prior to initiations of treatment. Global *Fgf21*$^{-/-}$ mice and *wild-type* littermates were bred in house and maintained on a HFHSD for 12 weeks prior to initiations of treatment. All mice were single- or group-housed on a 12:12-h light-dark cycle with free access to food and water.

METHOD DETAILS

Peptide Synthesis
Peptide backbones were synthesized by standard fluorenylmethoxycarbonyl (Fmoc)-based solid phase peptide synthesis using 0.1 mmol Rink amide 4-methylbenzhydrylamine (MBHA) resin (Midwest Biotech) on an Applied Biosystems 433A peptide synthesizer. The automated synthesizer utilized 20% piperidine in N-methyl-2-pyrrolidone (NMP) for N-terminal amine deprotection and diisopropylcarbodiimide (DIC)/6-CI-HOBt for amino acid coupling.

Synthesis of Glucagon/T$_3$ Conjugate
A 1:1 molar ratio of 3, 5, 3′-triiodothyronine and di-*tert*-butyl dicarbonate was dissolved in dioxane/water (4:1,v:v) in the presence of an ice bath with an addition of 0.1 equivalent of triethylamine (TEA). The reaction was stirred for 30 min at 30°C and then at room temperature for 30 hr, during which the progress of the reaction was monitored by analytical HPLC. Upon completion, the pH of the solution was lowered to 4.0 with 0.1 M hydrochloride (HCl) acid, subsequently treated it repetitively with dichloromethane (DCM) to extract desired product. The organic phase was collected, combined and evaporated in vacuum to afford crude product Boc-T$_3$-OH with good purity.

The peptide backbone synthesized contained a C-terminal N'-methyltrityl-L-lysine (Lys(Mtt)-OH) moiety, whose side chain was orthogonally deprotected by four sequential 10 min treatments with 1% trifluoroacetic acid (TFA), 2% triisopropylsilane (TIS) in DCM to expose an amine as a site for T$_3$ conjugation. The peptidyl-resin was then mixed with a 10-fold excess of Fmoc-L-Glu-OtBu(rE) activated by 3-(diethoxyphosphoryloxy)-1,2,3-benzotriazin-4(3H)-one/N,N-diisopropylethylamine (DEPBT/DIEA) in dimethylformide (DMF) for 2 hr. The completion of the coupling was confirmed by Kaiser test, after which the resin was washed and treated with 20% piperidine in DMF to remove the Fmoc protecting group located at the side chain of the γGlu residue. Subsequently, the peptidyl-resin was reacted with a 5-fold excess of crude Boc-T$_3$-OH combined with DEPBT/DIEA in DMF for 2 hr to facilitate T$_3$ conjugation to peptide backbone. Afterward, the resin were treated with TFA cleavage cocktail containing TFA/anisole/TIS/H$_2$O (85:5:5:5) for 2 hr at room temperature to release conjugate from solid support. Cleaved and fully deprotected conjugate was precipitated and washed with chilled diethyl-ether. The crude conjugates was dissolved in 15% aqueous acetonitrile containing 15% acetic acid and purified by preparative reversed-phase HPLC utilizing a linear gradient of buffer B over buffer A (A:10% aqueous acetonitrile, 0.1% TFA; B:100% acetonitrile, 0.1% TFA) on an axia-packed phenomenex luna C18 column (250 × 21.20mm) to afford the desired conjugate with carboxyl coupling of T$_3$ to glucagon.

Synthesis of Glucagon/iT$_3$ Conjugate
3, 5, 3′-triiodothyronine (Chem-Impex International Inc.) was solubilized in tert-butyl acetate in the presence of 0.1 equivalent of perchloric acid (HClO$_4$). The mixture was stirred at 0°C for 2 hr and at room temperature for 14 hr. Upon completion, the mixture was washed with water and ethyl acetate, treated with 10M sodium hydroxide (NaOH) until pH of the solution reached 9. Subsequently, the mixture was extracted with DCM. The combined organic phase was dried by magnesium sulfate (MgSO$_4$) and evaporated in vacuum to obtain the desired product NH$_2$-T$_3$-OtBu. NH$_2$-T$_3$-OtBu and succinic anhydride were mixed in anhydrous DMF with 0.1 equivalent of DIEA. The reaction was stirred at room temperature for 48 hr. The OH-Suc-T$_3$-OtBu product was obtained followed the same workup as described for NH$_2$-T$_3$-OtBu. Crude OH-Suc-T$_3$-OtBu was dissolved in 15% aqueous acetonitrile

containing 15% acetic acid and purified by semi-preparative reversed-phase HPLC using a linear gradient of buffer B over buffer A on an axia-packed phenomenex Luna C18 column (250 × 21.20mm).

Equimolar equivalents of HO-Suc-T_3-OtBu, DEPBT and DIEA were solubilized in DMF and directly added to the peptidyl-resin. The reaction was gently agitated at room temperature for two hours and was monitored by Kaiser test. The peptidyl resins were treated with TFA cleavage cocktail containing TFA/anisole/tTIS/H_2O (85:5:5:5) for 2 hr at room temperature to cleave conjugate from solid support. Cleaved conjugate was precipitated and washed with chilled diethyl-ether. The glucagon/iT_3 was dissolved and purified by reversed-phase HPLC using the condition described above.

Synthesis of Glucagon/rT_3 Conjugate

A 1:1 molar ratio of 3, 3′, 5′-triiodothyronine and di-*tert*-butyl dicarbonate were dissolved in dioxane/water (4:1,v:v) in the presence of an ice bath with an addition of 0.1 equivalent of TEA. The reaction was stirred for 30 min at 0°C and at room temperature for another 30 hr. Upon completion, the pH of the solution was lowered to 4.0 with 0.1 M HCl, subsequently treated it repetitively with DCM to extract desired product. The organic phase was collected, combined and evaporated in vacuum to afford crude product Boc-rT_3-OH with good purity.

The peptide backbone synthesized contained a C-terminal N'-methyltrityl-L-lysine (Lys(Mtt)-OH) moiety, whose side chain was orthogonally deprotected by four 10 min treatments with 1% TFA, 2% TIS in DCM to expose amine. The peptidyl-resin was then mixed with a 10-fold excess of Fmoc-L-Glu-OtBu (γGlu) activated by DEPBT/DIEA in DMF for 2 hr. The completion of the coupling was confirmed by Kaiser test, after which the resin was washed and treated with 20% piperidine in DMF to remove the Fmoc protecting group on the γGlu residue. Subsequently, the peptidyl-resin was reacted with a 5-fold excess of crude Boc-rT_3-OH combined with DEPBT/DIEA in DMF for 2 hr to facilitate rT_3 conjugation to peptide backbone. Afterward, the resin were treated with TFA cleavage cocktail containing TFA/anisole/TIS/H_2O (85:5:5:5) for 2 hr at room temperature to release conjugate from solid support. Cleaved and fully deprotected conjugate was precipitated and washed with chilled diethyl-ether. The glucagon/rT3 conjugate was dissolved and purified by reversed-phase HPLC using the same condition described above. We confirmed the molecular weights of peptide and conjugates by electrospray ionization (ESI) mass spectrometry and confirmed their character by analytical reversed-phase (HPLC in 0.1% TFA with an ACN gradient on a Zorbax C8 column (0.46 cm × 5 cm).

Human Glucagon Receptor Activation

Each peptide or conjugate was individually tested for its ability to activate the human GcgR through a cell-based luciferase reporter gene assay that indirectly measures cAMP induction. Human embryonic kidney (HEK293) cells were co-transfected with GcgR cDNA (zeocin-selection) and a luciferase reporter gene construct fused to a cAMP response element (CRE) (hygromycin B-selection). Cells were seeded at a density of 22,000 cells per well and serum deprived for 16 hr in DMEM (HyClone) supplemented with 0.25% (vol/vol) bovine growth serum (BGS) (HyClone). Serial dilutions of the peptides were added to 96-well cell-culture treated plates (BD Biosciences) containing the serum-deprived, co-transfected HEK293 cells, and incubated for 5 hr at 37°C and 5% CO_2 in a humidified environment. To stop the incubation, an equivalent volume of Steady Lite HTS luminescence substrate reagent (Perkin Elmer) was added to the cells to induce lysis and expose the lysates to luciferin. The cells were agitated for 5 min and stored for 10 min in the dark. Luminescence was measured on a MicroBeta-1450 liquid scintillation counter (Perkin-Elmer). Luminescence data were graphed against concentration of peptide and EC_{50} values were calculated using Origin software (OriginLab).

TR Transcriptional Activity

For testing of transcriptional activity HEPG2 cells were cultured in HAMF12/DEMEM medium (Biochrom), supplemented with 10 FBS. Cells were seeded at a density of 5 x10^4 cells/well in a 96 well plate. One day after seeding cells were transfect each with 0.45 ng of DR4-luciferase and TRalpha plasmids using Mefatektene (Biontex). Two days after transfection cells were stimulated with 1 μM of each compound for 10 hr. Reaction was stopped and luciferase activity was measured according to the manufactures protocol (Promega).

Plasma Stability

Each compound was incubated with phosphate buffered saline (PBS, pH = 7.4) containing 60% mouse plasma at 37°C for the duration of the study. At the time points of 6h, 24h and 72h, aliquots of the incubated solutions were withdrawn and diluted with acetonitrile to precipitate the plasma proteins, which were subsequently removed by microcentrifugation at 13,000 rpm for 5 min. The supernatant was collected and diluted for the analytical reversed-phase HPLC using a linear gradient of buffer B over buffer A (A: 10% aqueous acetonitrile, 0.1% TFA; B: 90% aqueous acetonitrile, 0.1% TFA) on a Zorbax C8 column (4.6 × 50mm).

RNA sequencing

RNA-Seq Total RNAs were extracted from frozen liver samples of 4 independent mice per group (vehicle, glucagon only, T_3 only, co-administration of glucagon and T_3 and glucagon/T_3) using TriPure RNA reagent (Sigma). Poly-A isolation, library generation and amplification were performed according to the protocol of the mRNA-Seq Library Prep Kit (Lexogen). The cDNA libraries were then converted to 5500 W libraries using the 5500 W Conversion Primer Kit (Lexogen). The Barcoded cDNA libraries were sequenced on a SOLiD 5500xl Wildfire sequencer (Life technology). Mapping of color-coded reads on the mouse genome (mm10 assembly) was

performed using the Lifescope software (Life Technologies). Reads for annotated (Ensembl) genes were counted using HtSeq. Normalization of expression levels for each gene and differential expression analysis were performed using DESeq2 (Love et al., 2014) (Bioconductor R package, false discovery rate < 5%). The synergy score (SS) was calculated as the relative fold change (FC) of (glucagon/T_3) compared to the maximum FC of T_3 and glucagon alone: SS = FC (glucagon/T_3) / max (T_3, glucagon). Synergistic hits were selected by a SS > 1.5. To reduce noise we removed transcripts from the hit list witch do not show significant regulation p < 0.05 (BH corrected) when treated with (glucagon/T_3) or opposite regulation.

Pathway Enrichment

Enriched KEGG pathways were determined using the hypergeometric distribution test using MATLAB (R2015b). Significant gene regulation was determined using DESeq2. Regulated genes used for pathway enrichment were selected using a threshold of p < 0.01 and the false detection rate corrected using Benjamini & Hochberg (BH) procedure. Among significant enriched KEGG pathways, relevant pathways were manually selected.

Rodent Pharmacological and Metabolism Studies

Compounds were administered by repeated s.c. injections in the middle of the light phase at the indicated doses with the indicated durations. Co-administration of compounds was administered by single formulated injections. Body weights and food intake were measured every day or every other day after the first injection. All studies with wild-type mice were performed with a group size of n = 8 or greater using mice on a C57Bl6j background. For assessment of glucose, pyruvate, and insulin tolerance during chronic treatment, the challenge tests were performed at least 24 hr after the last administration of compounds. For compound, insulin, and glucose tolerance tests, mice were fasted for 6 hr. For pyruvate tolerance tests, overnight fasting was employed. The investigators were not blinded to group allocation during the in vivo experiments or to the assessment of longitudinal endpoints.

Body Composition Measurements

Whole-body composition (fat and lean mass) was measured using nuclear magnetic resonance technology (EchoMRI).

Indirect Calorimetry

Energy intake, energy expenditure, respiratory exchange ratio, and home-cage activity were assessed using a combined indirect calorimetry system (TSE Systems). O_2 consumption and CO_2 production were measured every 10 min for a total of up to 120 hr (after 24 hr of adaptation) to determine the respiratory quotient and energy expenditure after an initial treatment regimen. Food intake was determined continuously for the same time as the indirect calorimetry assessments by integration of scales into the sealed cage environment. Home-cage locomotor activity was determined using a multidimensional infrared light beam system with beams scanning the bottom and top levels of the cage, and activity being expressed as beam breaks.

Blood Parameters

Blood was collected at the indicated times from tail veins or after euthanasia using EDTA- coated microvette tubes (Sarstedt), immediately chilled on ice, centrifuged at 5,000 g and 4°C, and plasma was stored at −80°C. For fast liquid performance chromatography (FPLC) of cholesterol distribution in different lipoprotein fractions, fresh plasma from each treatment group was pooled (n = 6-8) and ran over two Superose 6 HR columns in tandem. Cholesterol levels in the collected fractions were determined by colorimetric assay. Plasma insulin and T_3 were quantified by an ELISA assay (Ultrasenstive Mouse Insulin ELISA and Rodent T_3 ELISA; Alpco). Plasma FGF21 was quantified by an ELISA assay (Mouse FGF21 ELISA; Millipore). Plasma cholesterol, extracted hepatic cholesterol, triglycerides, ALT, and AST were measured using enzymatic assay kits (Thermo Fisher). Plasma creatinine and blood urea nitrogen were measured using enzymatic assay kits (Abcam). Plasma free fatty acids were measured using enzymatic assay kits (Wako). All assays were performed according to the manufacturers' instructions.

Histopathology

After chronic treatment, HFHCD-fed or HFHSD-fed C57Bl6/j male mice (age) were sacrificed with CO_2, body weight as well as heart weights and tibia length was taken during necropsy. Livers and whole hearts were embedded in paraffin using a vacuum infiltration processor TissueTEK VIP (Sakura). 3μm thick slides were cut using a HMS35 rotatory microtome (Zeiss) and H & E staining was performed. For H & E staining, rehydration was done in a decreasing ethanol series, rinsing with tapwater, 2min Mayers acid Hemalum, bluing in tapwater followed by 1min EosinY (both BioOptica). Dehydration was performed in increasing ethanol series, mounting with Pertex (Medite GmbH) and coverslips (CarlRoth Chemicals). The slides were evaluated independently using a brightfield microscope (Axioplan, Zeiss). Photos were taken using the Hamamatsu-Nanozoomer HT2.0 in 1.25x, 5x. 20x and 40x magnification. The hepatic steatosis score is defined as the unweighted sum of the three individual scores for steatosis, lobular inflammation and ballooning degeneration. Steatosis is graded by the presence of fat vacuoles in liver cells according to the percentage of affected tissue (0: < 5%; 1: 5%–33%; 2: 33%–66%; 3: > 66%). Lobular inflammation is scored by overall assessment of inflammatory foci per 200x field (0: no foci; 1: < 2 foci; 2: 2-4 foci; 3: > 4 foci). The individual score for ballooning degeneration ranges from 0 (none), 1

(few cells) to 2 (many cells). Total scores range from 0 to 8 with scores < 2 considered non-steatosis, 3 considered as borderline steatosis, 4-5 considered onset of steatosis, and > 6 considered steatosis.

Different to liver and heart, inguinal fat pad samples were embedded in paraffin using Leica embedding machine (EG1150 H) and cut in 5 μm sections using Leica Microtome (RM2255) to perform H&E staining. Samples were stained with hematoxyline for 4 min and eosinY for 2 min and fixed with Roti-Histokitt (Carl Roth) before analyzing them independently using Microscope Scope A.1 (Zeiss).

In Vivo Biodistribution Imaging

For whole body bio-distribution studies, male C57BL/6 mice (10-12 weeks of age) were housed in a controlled environment with water and chow provided *ad libitum*. Mice were subcutaneously injected with either a VivoTag750 labeled glucagon/T_3 conjugate ("glucagon*/T_3"; 100 nmoles kg^{-1}), a non-reactive 750nm fluorophore (100 nmol kg^{-1}; Genhance 750 Fluorescent Imaging Agent, PerkinElmer) or vehicle. After 1, 3, 6, 12, and 24 hr post injection, mice were sacrificed by cervical dislocation. Trunk blood (100 μL) was immediately collected into tubes containing 10 μl antiproteolytic cocktail (4.65 g EDTA + 92 mg aprotinin + 40,000 U heparin in 50 ml saline) for plasma preparation. Urine samples (10μl) were collected by puncturing the bladder using a syringe and a fine needle and immediately protected from degradation by adding 1μl of anti-proteolytic cocktail. Plasma and urine samples from all groups and time points were stored at 4°C for collective imaging on the same 96 well plate, 24 hr after injection and using an IVIS Spectrum instrument (Perkin Elmer). Stability of the 4°C stored samples was guaranteed by comparing the signal intensities with freshly prepared samples (data not shown). Besides blood and urine samples, organs were removed from all groups. All samples per time point were collectively imaged on the same petri dish. For data analysis, regions of interest (ROI) were drawn around the isolated organs, blood and urine spots to assess the epifluorescence signal emitted. Results were expressed as average radiant efficiency in units of photons/second within the region of interest [p/s/cm^2/sr]/[μW/cm^2]. Epifluorescent signals of the dye control and VivoTag750 labeled glucagon*/T_3 were corrected to the auto-fluorescent background signal of the time-matched vehicle control group.

Echocardiography

For transthoracic echocardiography, a Vevo2100 Imaging System (VisualSonics Inc., Toronto Canada) with a 30 MHz probe was used. All echocardiograms were performed on conscious animals to prevent anesthesia-related impairment of cardiac function as reported previously. Briefly, echocardiograms were obtained in parasternal long and short axis views. For accurate linear measurements of LV internal dimensions (LVID) and parasternal (LVPW) or septal (IVS) wall thicknesses, M-mode images of the heart in parasternal short-axis view at the level of the papillary muscle were acquired. Qualitative and quantitative measurements were made offline using analytical software (VisualSonics Inc.). Fractional shortening (FS) was calculated as FS% = [(LVIDd-LVIDs)/LVIDd] x 100. Ejection fraction (EF) was calculated as EF% = 100*((LVvolD-LVvolS)/LVvolD) with LVvol = ((7.0/(2.4+LVID)*LVID^3). The corrected LV mass (LV MassCor) was calculated as LV MassCor = 0.8(1.053*((LVIDd+LVPWd+IVSd)^3-LVIDd^3)). Heart rate and respiration rate were determined from M-mode tracings, using 3 consecutive intervals.

Rectal Body Temperature

Rectal body temperature was measured in conscious mice using a high-precision thermometer (thermosensor: Almemo ZA 9040, data logger: Almemo 2290-8, Ahlborn, Holzkirchen, Germany) that was carefully inserted into the rectum. Temperature of each individual was taken by the same researcher one hour after lights-on after chronic treatment *ab libitum*.

Atherosclerotic Plaque Assessment

The extent of atherosclerotic lesion formation was assessed in aortic root sections of Ldlr−/− mice that were treated with glucagon/T_3 or vehicle for 2 weeks by staining for lipid depositions with oil-red O. Briefly, atherosclerotic lesions were measured in 4-μm transverse cryo sections of aortic roots. Images of tissue sections were taken (Leica analysis software LAS) and quantified by manually outlining the lumen boundary. Subsequently, oil red O+ areas were outlined as well and the percentage of oil-red O+ areas in relation to the total area was calculated.

Immunohistochemistry For UCP1

iWAT samples were dissected and subsequently fixed and stored in 4% paraformaldehyde. After dehydration, tissues were embedded in paraffin and cut in 5 μm sections to perform immunohistochemistry using rabbit anti-UCP1 antibody (Abcam, ab10983). Therefore, samples were de-paraffinized and microwaved in citrate buffer (pH = 6) for antigen retrieval. To quench endogenous peroxidases samples were incubated with 3% hydrogen peroxide in methanol and then blocked with Avidin D, Biotin (Vectastain ABC Kit; Vector labs) and normal goat serum (10%). Anti-UCP1 antibody (1:400) was added and incubated over night, before applying secondary anti-rabbit antibody (1:300; Vector Labs ZA0324). Vectastain ABC reagent (Vectastain ABC Kit; Vector labs) was used followed by application of SIGMA*FAST* 3,3′-Diaminobenzidine (Sigma) for signal development, and subsequent counterstaining with hematoxylin and mounting. Finally, sections were analyzed using Microscope Scope A.1 (Zeiss).

Bone Density Measurements

Lumbar vertebrae L5 were analyzed using a SkyScan 1176 micro CT (Bruker, Billerica, USA) equipped with an X-ray tube working at 50 kV/100 μA. Resolution was 9 μm, rotation step was fixed at 1°, and a 0.5 mm aluminum filter was used. For reconstruction, region

of interest was defined from the middle of vertebral body, spanning 0.99 mm both direction to intervertebral discs. Trabecular bone volume/tissue volume (BV/TV), trabecular thickness (Tb.Th.), trabecular separation (Tb. Sp.), and trabecular number (Tb.N.) were determined according to guidelines by ASBMR Histomorphometry Nomenclature Committee.

Quantification of Accumulated T_3 In Liver and iWAT

The stock solutions of T_3 (Sigma Aldrich) and stable isotope-labled T_3 ($[^{13}C_6]T3$; Cambridge Isotope Laboratories) were prepared dissolving 5 mg of the standard in 100 ml of pure MeOH. T3 calibration standards that ranged in concentration from 0.5 pg/μL to 100 pg/uL were prepared from stock solution through dilution with a solvent mixture of 20% acetonitrile in water. $[^{13}C_6]T_3$ was prepared in a mixture of 20% acetonitrile in water at a concentration of 10 pg/μL. The calibration solutions as well as the internal standard solutions, were protected from light, stored at 4°C and wrapped with aluminum foil.

Tissue samples were homogenized in methanol containing an antioxidant solution (ascorbic acid, citric acid, and dithiothreitol at 25 g/L in methanol) by ultrasonication (Bandelin Electronics) 2 × 20 s under cooling with ice. Liquid-liquid extraction was performed as described in (Morreale de Escobar et al., 1985). Solid phase extraction was performed loaded the water phase into a SampliQ SPE cartridge (60 mg, 3 mL; Agilent Technologies), which were preconditioned sequentially with 3 ml of 50% a methanol in chloroform, 3 ml of pure methanol and 3 ml of water. The target compound as well as the internal standard were eluted with 0.6 ml of 0.1% formic acid in methanol. The solvent was evaporated to dryness under N_2 steam and then reconstituted in 0.3 ml of 0.1N HCl in water. The thyroid hormone derivatives were extracted back in organic solvent with 3 × 0.3 ml of ethyl acetate. The solvent was evaporated again and compounds re-dissolved in 60 μl in a mixture of 20% acetonitrile in water for instrumental analysis.

Compound separation was carried out on a nanoAcquity UHPLC system (Waters Corporation) interfaced with a quadrupole time-of-flight mass spectrometer Q-TOF2 (Waters-Micromass). The system was operated under MassLynx 4.1 software (Waters-Micromass) in QTOF-MS mode. Samples were infused at a flow rate of 5 μL/min and were monitored in positive ion electrospray mode. High purity nitrogen was used as de-solvation and auxiliary gas; argon was used as the collision gas. The de-solvation gas was set to 200 L/h at a temperature of 120°C, the cone gas was set to 50 L/h and the source temperature at 100°C. The capillary extraction and the cone voltages were set to 2.6 kV and 35 V respectively. The QTOF detector (MPC) was operated at 2100 V. The instrumentation ran in full-scan mode with the QTOF data being collected between m/z 100-1000 with a collision energy of 6 eV. The data were collected in the continuum mode with a scan time 1.5 s, interscan delay of 0.1 s. The processing of calibration and quantification data including peak integration, internal standard correction and linear regression was carried out using the QuanLynx Application Manager (Waters-Micromass).

A 5 μl volume of tissue sample was directly injected into an HSS-T3 micro-scale column: 300 μm i. d. x 150 mm length, 1.8 μm particle size (Waters Corporation) at a flow rate of 5 μL/min. The mobile phase was 0.1% formic acid in water (mobile phase A) and 0.1% formic acid in acetonitrile (mobile phase B). Gradient elution was performed according to the following elution program: 0-3 min, 95% A, 5% B; 3.5 min 70% A, 30% B; 5.5-6.5 min 62% A, 38% B; 7-10 min, 60% A, 40% B; 12-13 min 100% B, 13.5-20 min 95% A, 5% B. The temperature of the HSS-T3 column was kept at 40°C.

Gene Expression Analysis

Gene expression profiling in the liver, iWAT, eWAT, BAT, and heart were performed following treatment of mice according to the treatment paradigms explained in the figure legends for each specific analsysis. For tissue collection, mice were fasted for 4 hr and treated with compounds 2 hr prior to tissue collection. Gene expression was profiled with quantitative real-time RT–PCR using either TaqMan single probes or with specifically-designed TaqMan low-density array cards. The relative expression of the selected genes was normalized to the reference gene hypoxanthine-guanine phosphoribosyltransferase (*Hprt*).

QUANTIFICATION AND STATISTICAL ANALYSIS

Statistical parameters including the exact value of n, the definition of measures (mean ± SEM) and statistical significance are reported in the Figures and the Figure Legends. Data are judged to be statistically significant when $p < 0.05$ by 1-way or 2-way ANOVA, where appropriate, and markers for significance are defined in the Figures and the Figure Legends. Statistical analysis was performed in Graph Pad PRISM.

DATA AND SOFTWARE AVAILABILITY

Data Resources

Raw data files for the RNA sequencing analysis have been deposited in the NCBI Gene Expression Omnibus under accession number GEO: GSE85793.
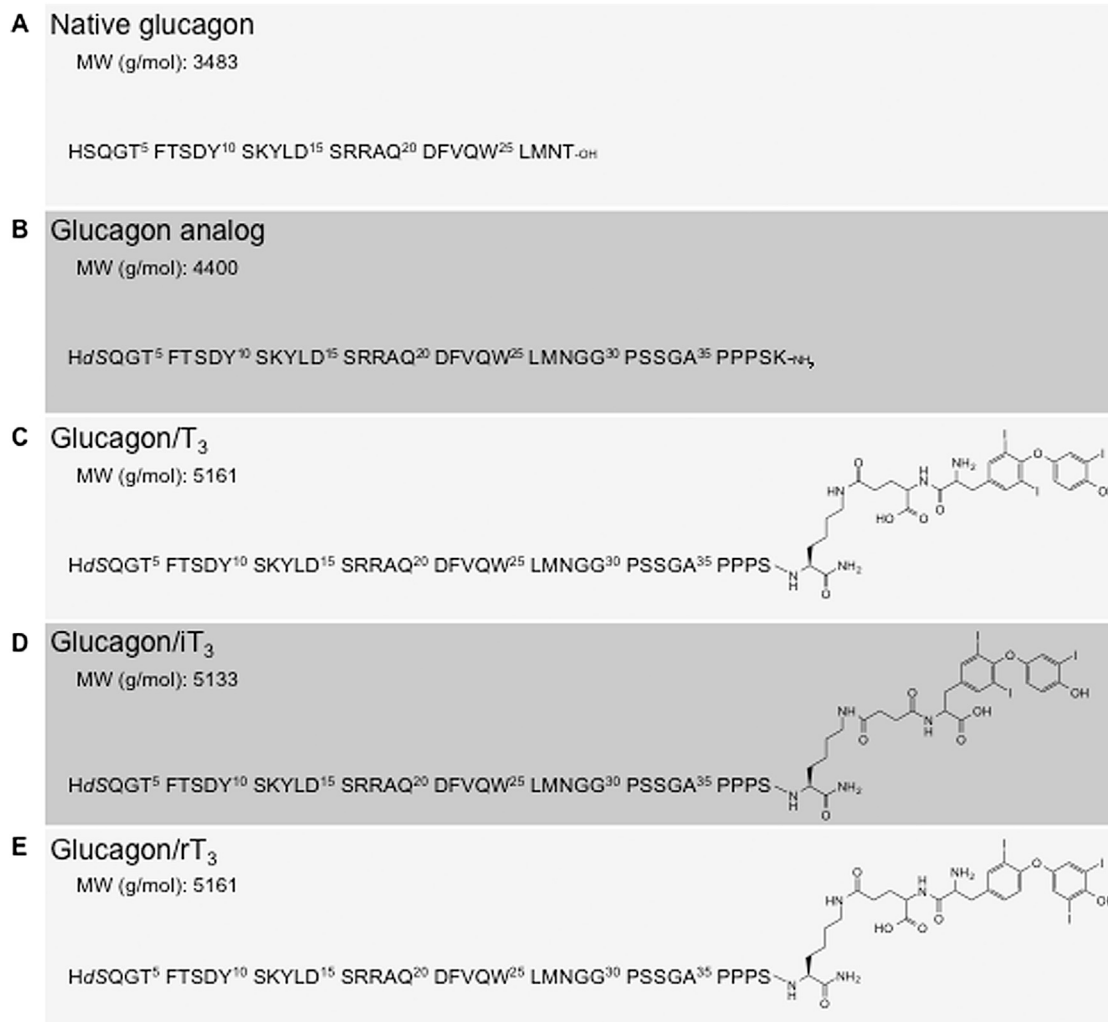
Figure S1. Chemical Structures of Glucagon and T_3 Conjugates, Related to Figure 1

Sequence, structure, molecular weight and GcgR activity of (A) native glucagon, (B) the glucagon analog used for creation of conjugates, (C) glucagon/T_3, (D) glucagon/iT_3, and (E) glucagon/rT_3.
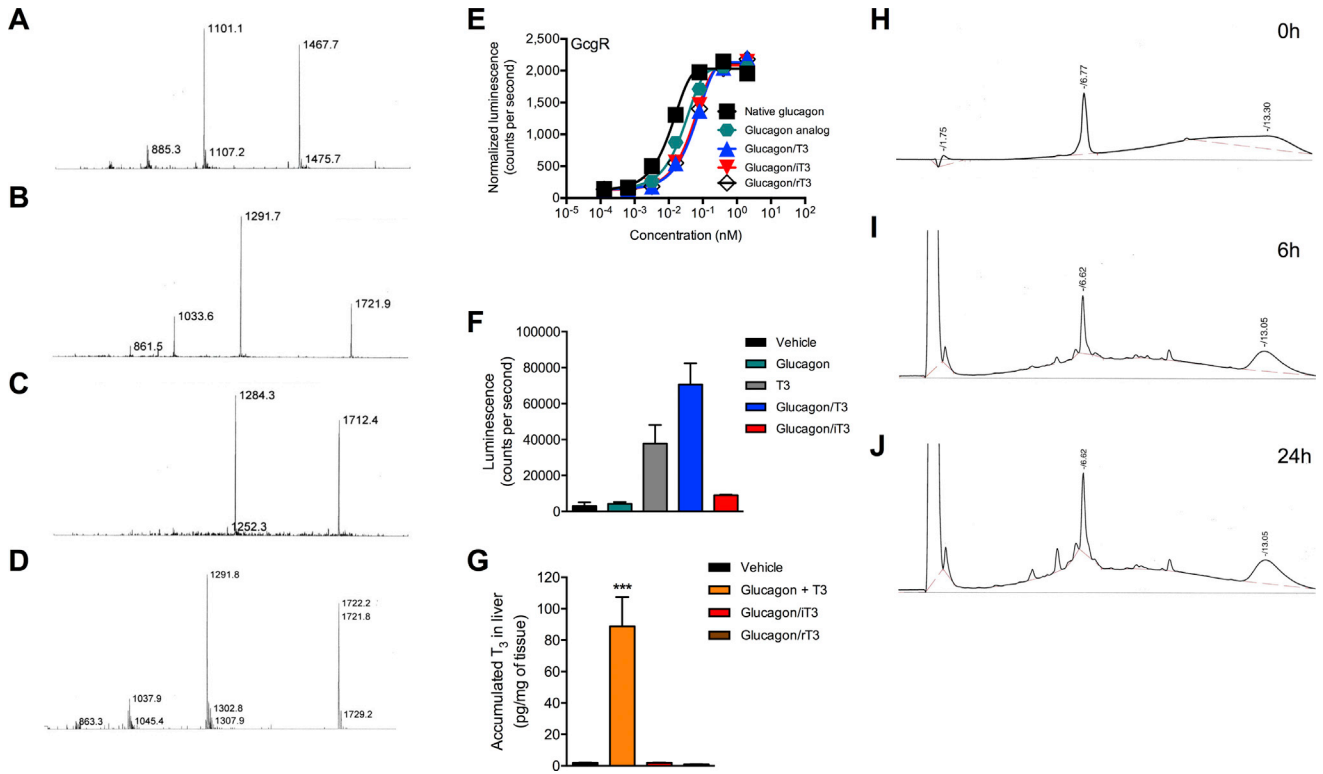
Figure S2. In Vivo and In Vitro Profiling of Glucagon/T_3 Character, Constituent Receptor Activity, and Stability, Related to Figure 1

Mass spectrometry confirming the identity of (A) the glucagon analog, (B) glucagon/T_3, (C) glucagon/iT_3, and (D) glucagon/rT_3. Receptor activity profiles of the conjugates at (E) GcgR and (F) THR using DR4-luciferase reporter assays. (G) Effects on T3 levels in the livers of HFHSD fed C57Bl6j male mice following daily s.c. injections of vehicle (black), equimolar co-administration of the glucagon analog and T_3 (orange), glucagon/iT_3 (red), or glucagon/rT_3 (brown) at a dose of 100 nmol kg^{-1} for 7 days (n = 8).

HPLC chromatograms of glucagon/T3 incubated in human plasma at 37°C after (H) 0 hr, (I) 6 hr, and (J) 24 hr exposure.

***p < 0.001 comparing effects following compound injections to vehicle injections
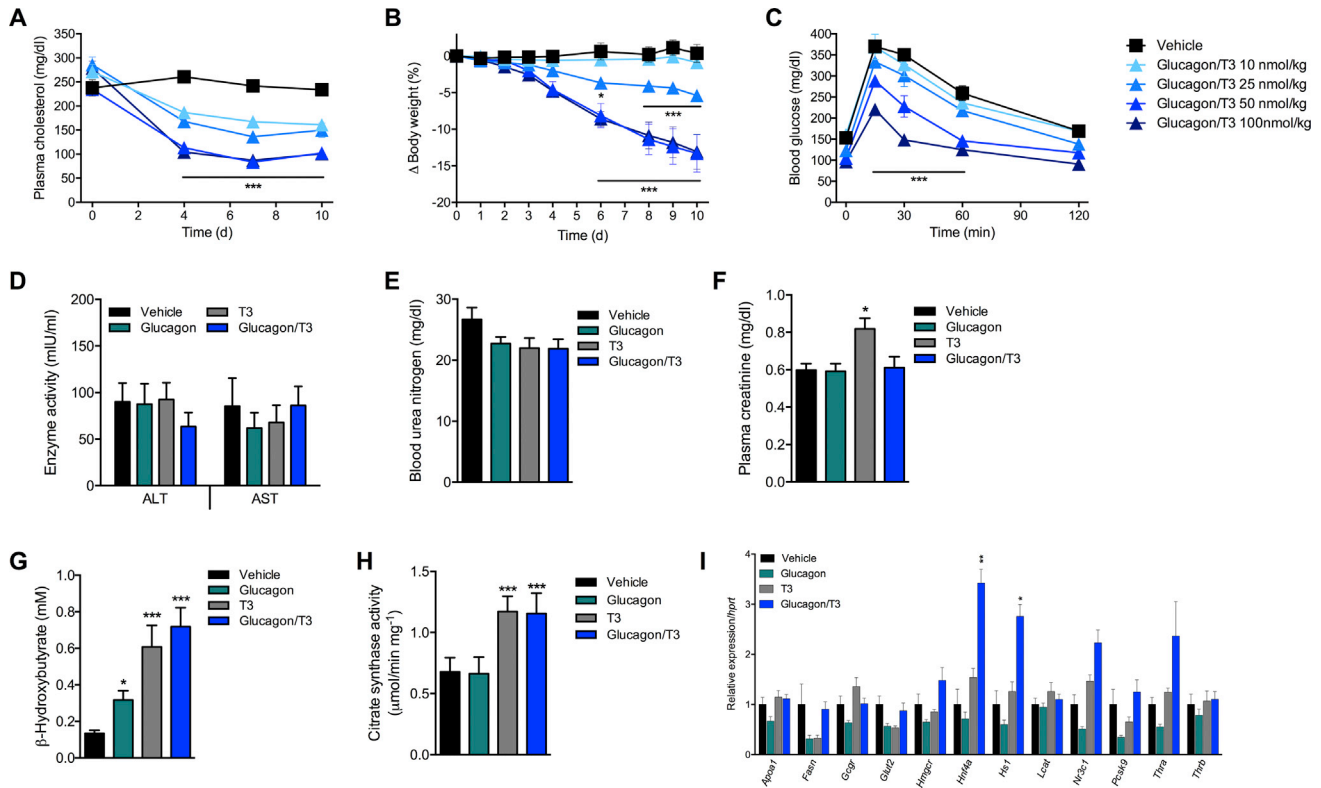
Figure S3. Glucagon/T3 Dose-Dependently Improves Metabolic Parameters and Glucagon/T₃ Does Not Harm Tissue Function, Related to Figures 1, 4, 5, and 6

(A-C) Effects on (A) plasma levels of cholesterol over time, (B) body weight change, and (C) intraperitoneal glucose tolerance (1.5 g kg^{-1}) in HFHSD-fed male C57Bl6j mice following daily s.c. injections of vehicle (black) or glucagon/T$_3$ at a dose of 10, 25, 50 or 100 nmol kg^{-1} (increasing shades of blue) for 10 days (n = 8). Effects on plasma levels of (D) ALT and AST, (E) blood urea nitrogen, (F) creatinine and (G) β-hydroxybutyrate, (H) hepatic citrate synthase activity, and (I) hepatic mRNA expression, from HFHCD-fed male C57Bl6j mice following daily s.c. injections of vehicle (black), a glucagon analog (teal), T$_3$ (gray), or glucagon/T$_3$ (blue) at a dose of 100 nmol kg^{-1} for 14 days (n = 8).
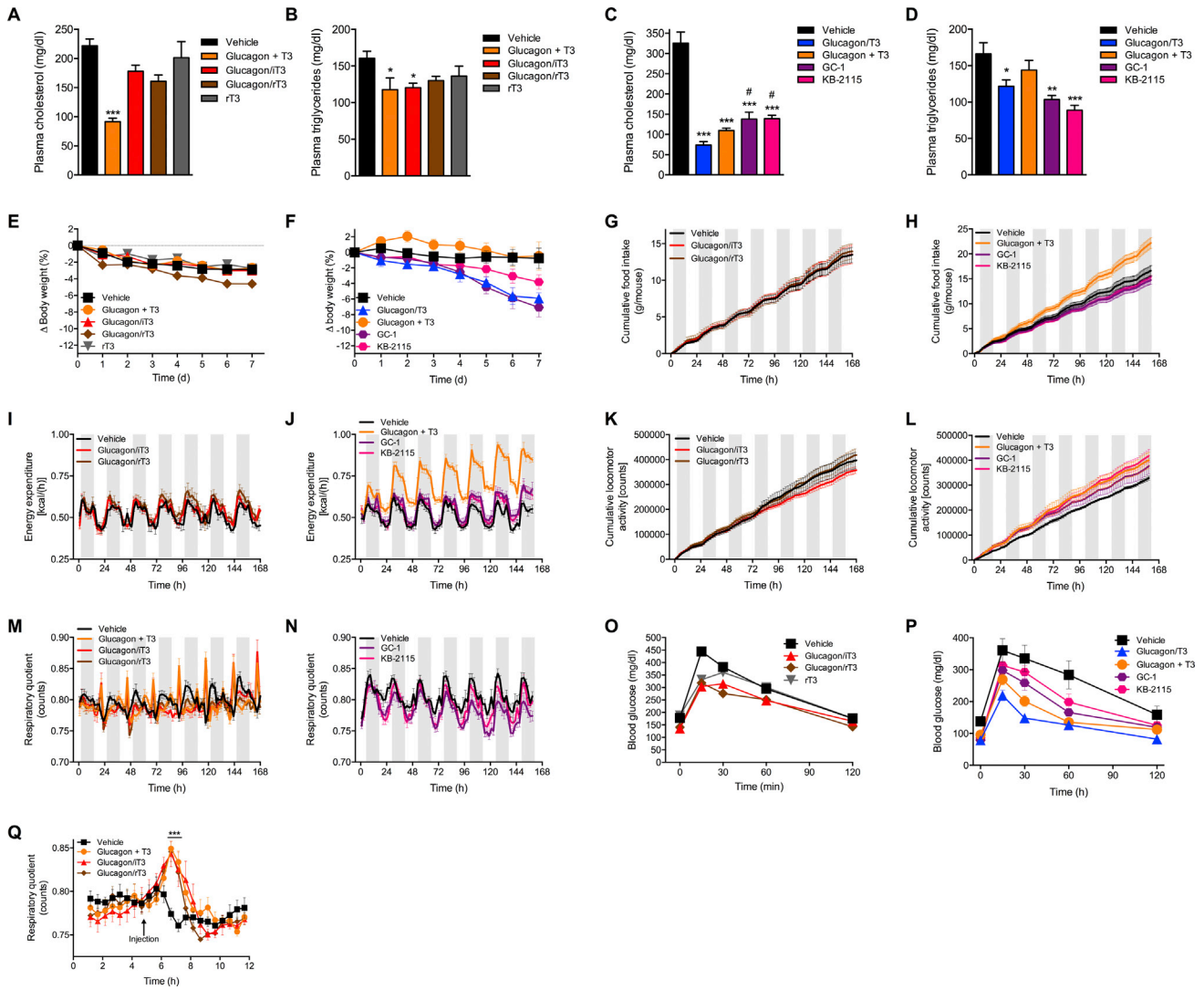
Figure S4. Metabolic Efficacy of Different Glucagon/T₃ Conjugate Versions, Co-administration, and Thyromimetics, Related to Figures 1, 4, 5, and 6

Effects on plasma levels of (A,C) total cholesterol, (B,D) triglycerides, (E,F) percent body weight loss, (G,H) cumulative food intake, (I,J) longitudinal energy expenditure, (K,L) cumulative locomotor activity, (M,N) longitudinal respiratory quotient, (O,P) intraperitoneal glucose tolerance (1.5 g kg⁻¹), and (Q) acute effects on RER during the light phase of the second day of treatment from HFHSD-fed male C57Bl6j mice following daily s.c. injections of vehicle (black), equimolar co-administration of the glucagon analog and T₃ (orange), glucagon/iT₃ (red), glucagon/rT₃ (brown), rT₃ (gray), GC-1 (purple) or KB-2115 (pink) at a dose of 100 nmol kg⁻¹ for 7 days (n = 8).

*p < 0.05 and ***p < 0.001 comparing effects following compound injections to vehicle injections.

All data are presented as mean ± SEM.
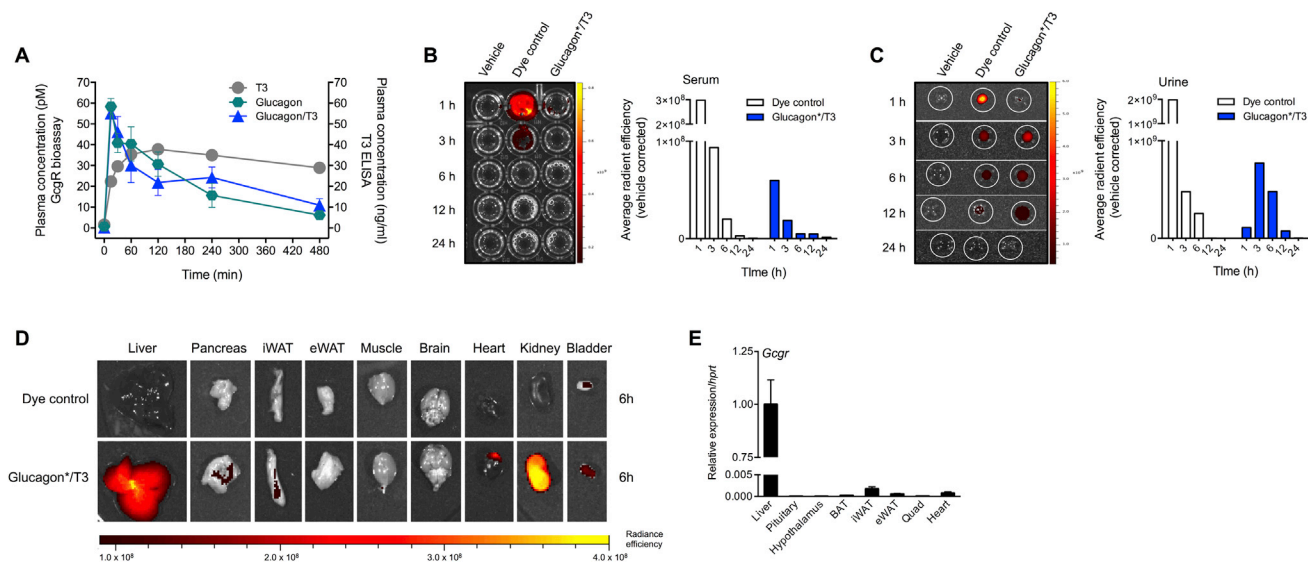
Figure S5. Pharmacokinetics and Biodistribution Are Driven by the Glucagon Component of the Conjugate, Related to Figure 2

(A) Effects on plasma concentrations of the different therapies following a single s.c. injection of a glucagon analog (teal), T_3 (gray), or glucagon/T_3 (blue) at a dose of 100 nmol kg^{-1} in lean chow-fed rats (n = 8). Plasma concentrations of glucagon and glucagon/T_3 were measured by a GcgR activity bioassay and plasma concentrations of T_3 were measure by a ELISA system for total T_3.

(B and C) Epifluorescent signal and quantified average radiant efficiency of (B) plasma and (C) urine over time following a single s.c. injection of vehicle, unconjugated dye control, or fluorescently labeled glucagon/T_3 (glucagon*/T_3) at a dose of 100 nmoles kg^{-1} in lean, chow-fed C57Bl6j mice.

(D) Epifluorescent signal from different tissues collected 6h after a single s.c. injection of vehicle, unconjugated dye control, or fluorescently labeled glucagon/T_3 (glucagon*/T_3) at a dose of 100 nmoles kg^{-1} in lean, chow-fed C57Bl6j mice. The liver samples are the same from (Figure 2A).

(E) Relative expression of *Gcgr* in various tissues harvested from lean, chow-fed C57Bl6j mice.

All data are presented as mean ± SEM.
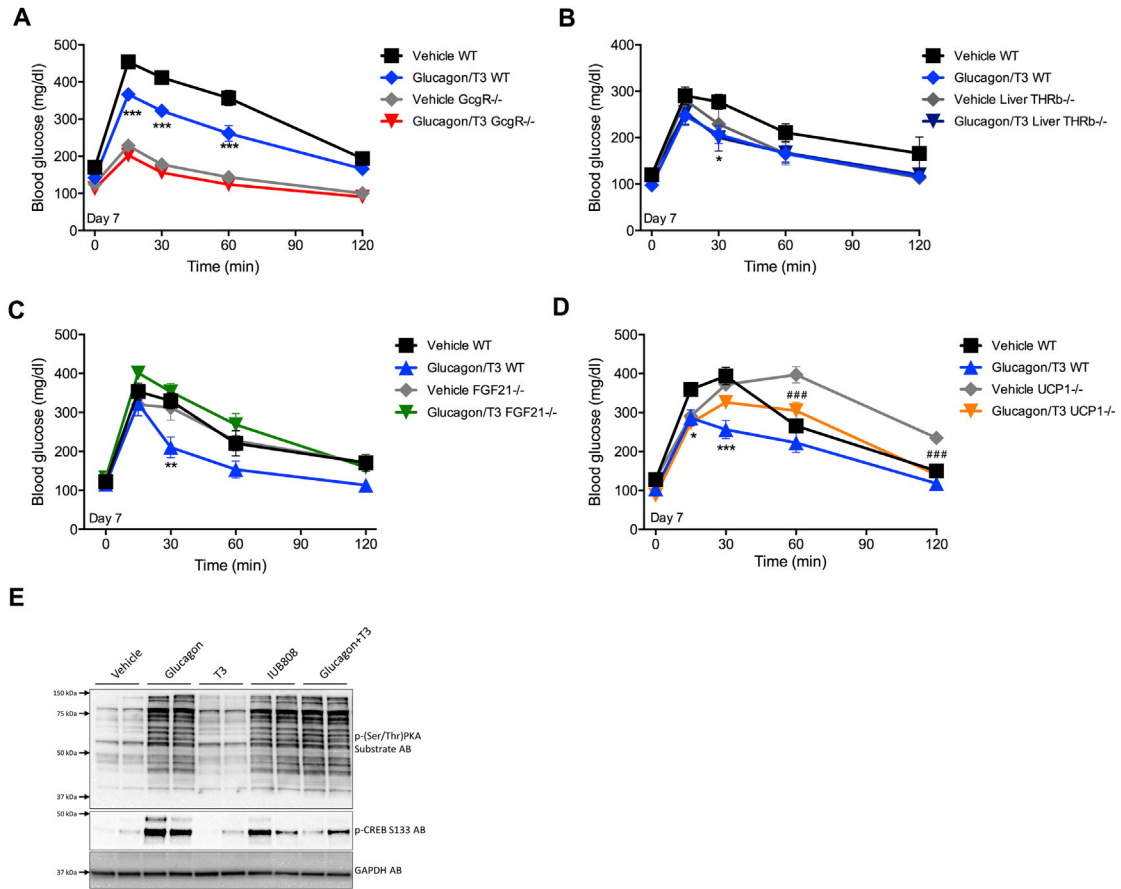
Figure S6. T$_3$ Alters Downstream GcgR Signaling, Related to Figure 6

Effects on chronic (after 7d of therapy) intraperitoneal glucose tolerance (1.5 g kg^{-1}) in (A) HFHSD-fed global GcgR$-/-$ male mice, (B) HFHCD-fed Alf-THRβ$-/-$ male mice, (C) HFHSD-fed global FGF21$-/-$ male mice, and (D) HFHSD-fed global UCP1$-/-$ male mice following daily s.c. injections of vehicle (black) or glucagon/T$_3$ (blue) at a dose of 100 nmol kg^{-1} (n = 5-9). (E) Representative western blot showing the acute effects on levels of phosphorylated PKA and CREB normalized to GAPDH in livers of lean C57Bl6j mice 15 min following a s.c. injection of vehicle, a glucagon analog, T$_3$, glucagon/T$_3$, or glucagon and T$_3$ co-administration at a dose of 100 nmol kg^{-1} (n = 8)

*$p < 0.05$, **$p < 0.01$, and ***$p < 0.001$ comparing effects following compound injections to vehicle injections within each respective wild-type genotype. ###$p < 0.001$ comparing effects following compound injections to vehicle injections within each respective knockout genotype
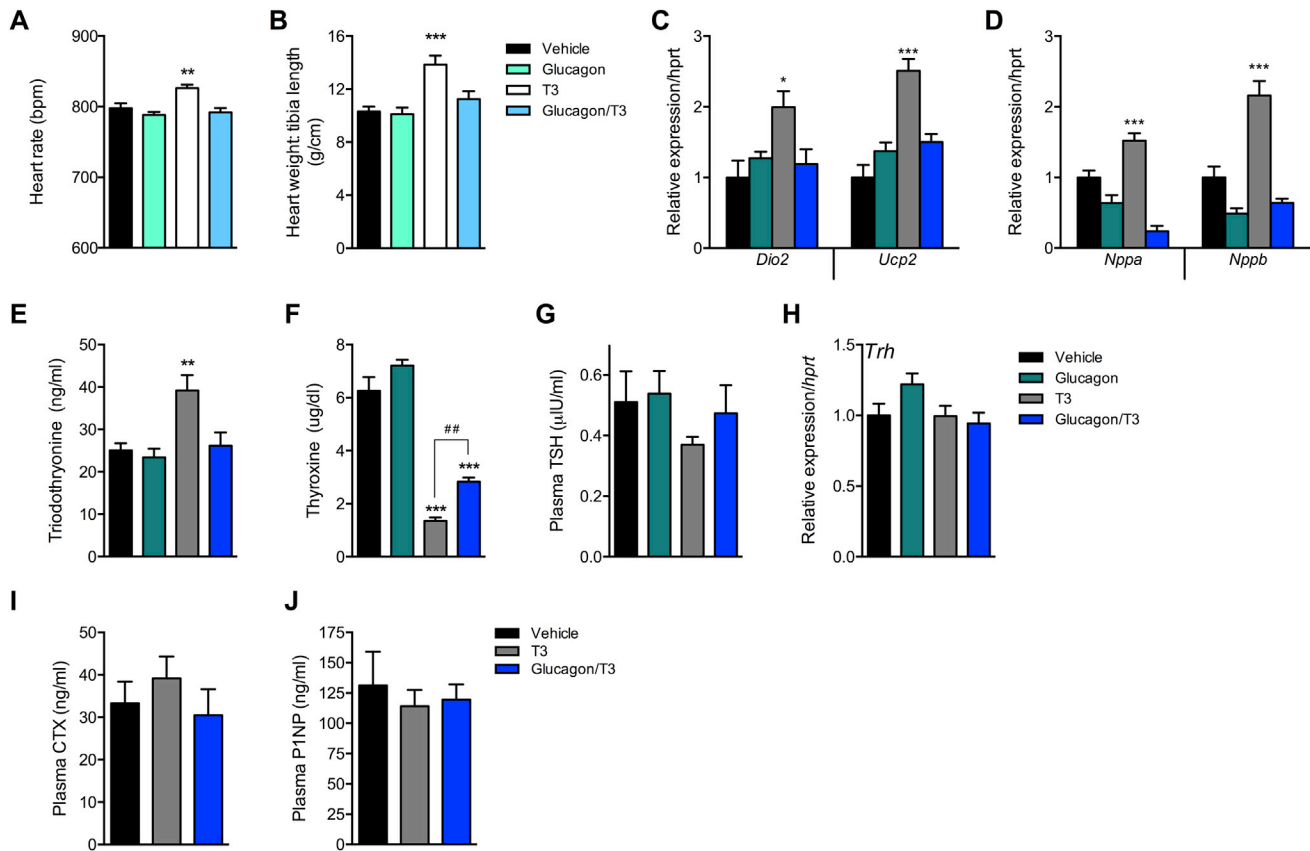
Figure S7. Low Dose T₃ Causes Tachycardia and Cardiac Hypertrophy whereas Glucagon/T₃ Is Devoid of Adverse Effects on Cardiac Function, Related to Figure 7

(A and B) Effects on (A) heart rate as measured by unrestrained electrocardiography and (B) heart weight to tibia length ratio from HFHSD-fed male C57Bl6j mice following daily s.c. injections of vehicle (black), a glucagon analog (light teal), T₃ (white), or glucagon/T₃ (light blue) at a dose of 10 nmol kg⁻¹ (n = 8) for 28 days.

(C and D) Effects on whole heart mRNA expression of (C) T₃-sensitive targets and (D) surrogate hypertrophic markers from HFHSD-fed male C57Bl6j mice following daily s.c. injections of vehicle (black), a glucagon analog (teal), T₃ (gray), or glucagon/T₃ (blue) at a dose of 100 nmol kg⁻¹ (n = 8) for 28 days.

(E–H) Effects on plasma levels of (E) total triiodothyonine, (F) total thyroxine, and (G) TSH, and (H) hypothalamic mRNA expression of *Trh* from HFHCD-fed male C57Bl6j mice following daily s.c. injections of vehicle (black), a glucagon analog (teal), T₃ (gray), or glucagon/T₃ (blue) at a dose of 100 nmol kg⁻¹ for 14 days (n = 8).

(I and J) Effects on plasma levels of (I) CTX and (J) P1NP from lean C57Bl6j mice following a s.c. injection of vehicle (black), a glucagon analog (teal), T₃ (gray), or glucagon/T₃ (blue) at a dose of 25 nmol kg⁻¹ for 14 days (n = 8).

*p < 0.05, **p < 0.01, and ***p < 0.001 comparing effects following compound injections to vehicle injections unless otherwise indicated.

All data are presented as mean ± SEM.